Journal of Archaeological Science 86 (2017) 81–100

Contents lists available at ScienceDirect

Journal of Archaeological Science

journal homepage: http://www.elsevier.com/locate/jas

Heat-induced alteration of glauconitic minerals in the Middle Stone Age levels of Blombos Cave, South Africa: Implications for evaluating site structure and burning events

Magnus M. Haaland [a, *], David E. Friesem [b], Christopher E. Miller [c, d], Christopher S. Henshilwood [a, e]

[a] Department of Archaeology, History, Cultural Studies and Religion, University of Bergen, Øysteinsgate 1, PO Box 7805, N-5020 Bergen, Norway
[b] McDonald Institute for Archaeological Research, University of Cambridge, Downing Street, Cambridge CB2 3ER, UK
[c] Institute for Archaeological Sciences, University of Tübingen, Rümelinstr. 23, 72070 Tübingen, Germany
[d] Senckenberg Center for Human Evolution and Paleoenvironment, University of Tübingen, Rümelinstr. 23, 72070 Tübingen, Germany
[e] Evolutionary Studies Institute, University of the Witwatersrand, P.O. WITS, 2050 Johannesburg, South Africa

ARTICLE INFO

Article history:
Received 22 February 2017
Received in revised form
5 June 2017
Accepted 11 June 2017
Available online 27 June 2017

Keywords:
Middle Stone Age
Site structure
Hearth
Combustion feature
Fire proxy
Fire experiment
FTIR
Micro-FTIR
Spatial analysis
GIS
Colourimetry
Micromorphology

ABSTRACT

In this paper we conduct geochemical and colourimetric measurements of glauconite grains in micromorphological thin sections from the Middle Stone Age site of Blombos Cave, South Africa, to investigate the formation, internal structure and reworking of heat-exposed cave deposits that are related to prehistoric burning events. Controlled heating experiments were first carried out on glauconite-rich loose sediments and block samples, both of which were collected from the Blombos Cave bedrock. The control samples were then subjected to Fourier transform infrared spectrometry (FTIR), microscopic Fourier transform infrared spectrometry (micro-FTIR) and petrographic-colourimetric analyses. The control experiment shows that glauconitic minerals undergo a gradual and systematic colour change when temperatures reach higher than c. 300–400 °C, primarily due to dehydration and iron oxidation. They also undergo clear structural changes when temperatures reach higher than c. 550 °C due to dehydroxylation and mineral transformation. By assessing the nature and degree of heat-induced optical and molecular alteration in glauconitic minerals, we demonstrate how glauconite grains in thin sections can be classified by the temperature to which they were exposed (20–400 °C, >400 °C, >600 °C and >800 °C). To assess the archaeological relevance of our controlled heating experiment, we applied this glauconite classification scheme to >200 grains found in three micromorphological thin sections of a Middle Stone Age (MSA) combustion feature. These grains were individually geo-referenced within the local coordinate system of Blombos Cave, through a thin-section-based GIS mapping procedure. With improved spatial control, we were able to study both the general distribution of non-altered and heat-altered glauconite grains in their original sedimentary context, as well as to calculate heat distribution models that cover the entire sampled section. This combined geo-chemical, optical and spatio-contextual approach provides insights into more elusive aspects of MSA site structure and burning events, such as heat intensity, burning frequency, temperature distribution, internal hearth structure and post-depositional reworking. The workflow we propose may easily be implemented and adapted to other archaeological contexts and to analogous sedimentary materials that show comparable heat-induced alteration patterns.

1. Introduction

Archaeologists routinely use the presence or absence of evidence for fire, as well as the size, placement and frequency of hearths, to infer prehistoric site structure and fire-related human activities (e.g. Henry et al., 1996; Wadley, 2006; Vallverdú et al.,

* Corresponding author.
E-mail address: magnus.haaland@uib.no (M.M. Haaland).

http://dx.doi.org/10.1016/j.jas.2017.06.008

2012; Shahack-Gross et al., 2014). However, several studies demonstrate that our ability to properly recognise and evaluate burnt contexts, macroscopically in the field, can be limited (Mentzer, 2012; Mallol et al., 2013). At some sites an intact, unlined open hearth can only be recognised by the presence of a reddened substrate, overlain by thin layers of charcoal and ash constituting a predictable trifold structure (Canti and Linford, 2000; Mentzer, 2012; Friesem et al., 2014b). Yet at many sites, as in the case of the Middle Stone Age (MSA) and Later Stone Age (LSA) layers at Blombos Cave, South Africa (Fig. 1), the identification of a structurally intact hearth versus a post-depositionally disturbed, redeposited or mixed burnt deposit can be more difficult, since the physical preservation of burnt deposits is variable and the quartz-rich substrate does not easily rubify.

Blombos Cave is located in Blombosfontein Nature Reserve (3.5 km2), c. 300 km east of Cape Town on the southern coast of South Africa (Fig. 1a). The lower part of the 3 m deep cave sequence is comprised of laminated deposits that contain MSA artefacts and features dated to ca. 101–70 ka (Fig. 1b and c) (Henshilwood et al., 2011; Jacobs et al., 2013). Several unlined, discrete hearths, combustion features and other fire-related deposits containing ash, charcoal and burnt sediments have been documented within the MSA deposits (Henshilwood et al., 2001; Henshilwood, 2005). While the charcoal shows variable preservation, much of the original ash has recrystallized and mixed with the calcareous-rich matrix. In addition, numerous millimetre thick lenses of black, humified and non-burnt material are frequently encountered within the cave deposits. In the field, the appearance of these black lenses is similar to that of burnt or charred material. Consequently, it is hard to tell from the location and nature of macroscopic observations whether specific deposits inside the cave truly were burnt, whether they were burnt *in-situ* or whether they could have been reworked or redeposited.

Many studies have, however, demonstrated that heat exposed sediments, e.g. sediments directly below an open fire, show indications of having been altered when examined microscopically (Canti and Linford, 2000; Berna et al., 2007; Karkanas et al., 2007; Mallol et al., 2007; Berna et al., 2012; March et al., 2014; Shahack-Gross et al., 2014; Aldeias et al., 2016). In a number of archaeological contexts, the effects of high temperatures on the molecular structure of sedimentary components has been successfully examined using both bench Fourier transform infrared spectrometry (FTIR) on bulk samples (Weiner, 2010) and microscopic FTIR (micro-FTIR) on thin sections (e.g. Berna et al., 2012; Goldberg et al., 2012; Shahack-Gross et al., 2014; Villagran et al., 2017).

The sedimentary infilling of Blombos Cave is driven partly by the granular disaggregation of the cave wall and ceiling, and partly by input from exterior aeolian processes. The cave is formed in the Mio-Pliocene shallow marine and aeolian deposits of the De Hoopvlei and the Wankoe formations (Malan, 1990; Malan et al., 1994) and the interior sediments thus consist primarily of unconsolidated, calcareous quartz-rich silt and sand. We also find a high abundance (>100 per 1 cm^2) of green, sand-sized and pellet-shaped minerals that derive from the bedrock and that are randomly distributed within the excavated deposits (Fig. 2). Based on their optical characteristics and a comparison of their FTIR spectra with published spectra, we confirmed that they are glauconitic minerals (see Fig. 3 and Table 1; Odin et al., 1988; Chukanov 2014).

Similar to many sheet silicate minerals, glauconite grains can alter their colour and chemical composition due both to weathering processes (McRae, 1972; Pestitschek et al., 2012) and exposure to heat (Ramaswamy and Kamalakkannan, 1995; Hajpál and Török, 2004; Pavlyukevich et al., 2005; Basso et al., 2008). Encouraged by the abundance of glauconitic grains within the Blombos Cave deposits and confronted with the preservation state and complexity of the combustion features at this site, the aim of this study is to investigate a new proxy (glauconite) to examine site formation processes associated with prehistoric burning events, and to develop a spatio-contextual framework in which this proxy can be practically applied to oriented archaeological sediment samples. Our specific objectives are threefold:

(1) Identifying and characterizing burnt glauconite grains, using geological control samples heated to known temperatures as a reference;
(2) Reconstructing the temperatures to which grains in archaeological thin sections were exposed, using FTIR, micro-FTIR and petrographic colourimetry;
(3) Mapping the spatial distribution of burnt and unburnt glauconitic grains in the archaeological samples, by importing geo-referenced, high-resolution thin section scans and orthophographic sections photos into a GIS application.

To demonstrate this framework's potential in identifying and evaluating prehistoric fire and burning events, we include a case study on a micromorphological block sample collected from a combustion feature in the lower part of the MSA sequence in Blombos Cave (BBC-13-14).

2. Properties of glauconitic minerals

2.1. Mineralogy and chemical properties

Glauconite belongs to a group of compositionally heterogeneous, dioctahedral, potassium and iron-rich phyllosilicates, with the general chemical formula: (K,Na) (Mg,Fe^{2+},Fe^{3+}) (Fe^{3+},Al) $(Si,Al)_4O_{10}(OH)_2$. In the structure of glauconitic mica, each layer consists of two silica tetrahedral sheets facing one central octahedral sheet (similar to 2:1 type clay minerals) (Grim, 1968; Odin et al., 1988; Dooley, 2006). In a fresh state, glauconitic grains show an ovoidal or spheroidal morphology and range in size from 1 mm (coarse sand) to clay size. The colour of glauconitic minerals range from dark olive or pale green (fresh) to yellowish or brownish green (weathered) in plane polarized light (Dooley, 2006; Basso et al., 2008; Pestitschek et al., 2012). The nuances in the green colour are related to the relative amounts of iron and aluminium present in the mineral, as well as the ratio between the divalent and trivalent iron ions (McRae, 1972). McRae (1972) reports that oxidation of structural iron due to natural weathering, especially in soils, can cause the glauconite grains to produce a heterogeneous, rusty-brown colour. The rusty parts are primarily distributed around the rim of the grain, or along weathering-induced cracks that often disrupt the grain's pellet-shaped morphology (cf. supplementary fig. A.1 for weathered grains from Blombos Cave). In South African contexts, the occurrence of “black glauconite” pellets have previously been reported by Wigley and Compton (2007), yet these grains also show a distinct green colour in thin section (Compton, John, Personal Communication, E-mail, April 21, 2017).

2.2. Infra-red spectra (transmission) of glauconite

Many researchers have studied the IR spectra of Fe–Mg dioctahedral micas (e.g. Farmer, 1974; Marel et al., 1976; Slonimskaya et al., 1986; Odin, 1988; Chukanov 2014), including archaeologists (Affonso and Pernicka, 2001), and they have reported that in glauconite, high-frequency absorption bands are observed around 3600 cm^{-1} (υ $Al^{3+}.Mg^{3+}$ –OH), 3560 cm^{-1} (υ $Fe^{3}+.Fe^{3+}/Fe^{3+}.Mg^{2+}$ –OH) and 3535 cm^{-1} (υ $Fe^{3+}.Fe^{2+}$ –OH); all of which have been associated with the stretching vibrations of hydroxyl groups (cf. Fig. 1 and Table 1). A broad and variable band near 3400 cm^{-1} has

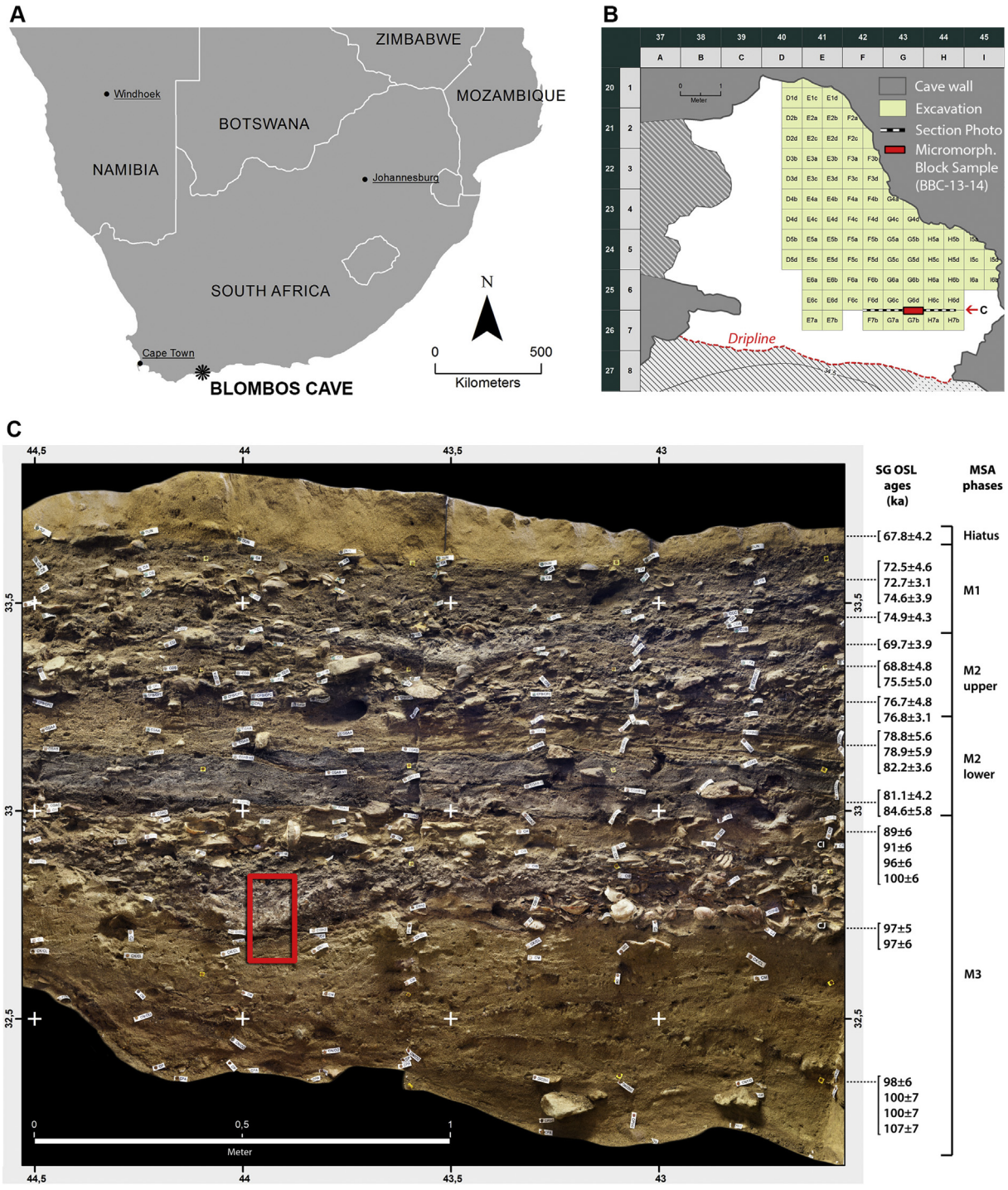

Fig. 1. (a) Location of Blombos Cave, South Africa; (b) Excavation plan of Blombos Cave and sampling location; (c) Orthophoto of the southern section of Blombos Cave. Red square indicating location of the micromorphological block sample collected from a 1 m wide, 0.3 m deep ash rich feature in unit CIBh2. (For interpretation of the references to colour in this figure legend, the reader is referred to the web version of this article.)

been linked to H_2O absorption (υ H_2O) (Odin et al., 1988).

The absorption between 1200 cm^{-1} and 400 cm^{-1} in glauconite is related to both the OH-bending vibrations of the tetrahedral sheets, as well as the absorption modes of the octahedral sheets. Most notable is the presence of a strong band at 960 cm^{-1} which is assigned to in-plane Si–O–Si stretching vibrations (Odin, 1988). The absorption bands around 815 cm^{-1} and 680 cm^{-1} have been assigned to the out-of-plane bending vibrations of hydroxyl groups that are in coordination with Fe^{3+} and Mg cations (Odin et al., 1988). Si–O bending vibrations cause absorption in the frequency range between 540 cm^{-1} and 400 cm^{-1}, but the specific frequencies vary greatly and according to the composition of the octahedral sheet (peaks are typically found at 489 cm^{-1}, 460 cm^{-1} and 431 cm^{-1}).

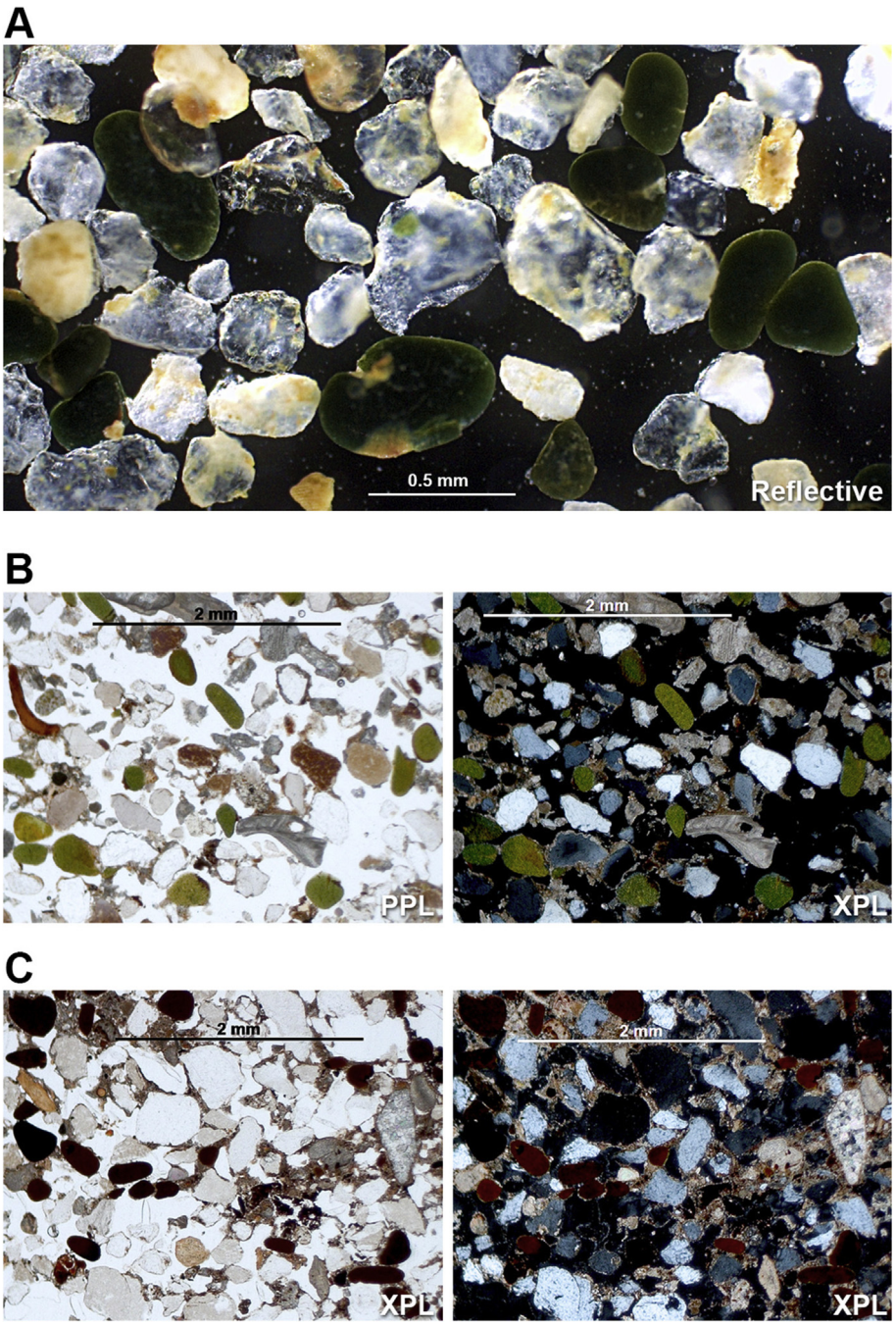

Fig. 2. Photomicrographs of glauconitic grains from Blombos Cave. (a) Smear mount of bedrock sample showing green, pellet-shaped glauconitic minerals (reflective light); (b) Thin section of green glauconitic grains in a calcareous, sandy matrix (XPL and PPL, 25x); (c) Thin section of red and black glauconite grains found in a burnt and ash rich matrix (XPL and PPL). (For interpretation of the references to colour in this figure legend, the reader is referred to the web version of this article.)

2.3. Thermal characteristics of glauconite

Heat-induced molecular alteration of glauconitic minerals have been widely studied, primarily through Mössbauer spectroscopy, X-ray diffraction (XRD), thermal analysis, and X-ray fluorescence (XRF); sometimes in combination with Fourier transform infrared (FTIR) spectroscopy (McRae, 1972; Smykatz-Kloss, 1974; Marel et al., 1976; Heller-Kallai and Rozenson, 1980; MacKenzie et al., 1989; Muller et al., 2000; Affonso and Pernicka, 2001; Pavlyukevich et al., 2005).

Differential-thermal analysis of glauconitic minerals shows curves indicative of weight loss between c. 80 °C and 260 °C and between c. 430–825 °C (McRae, 1972; Smykatz-Kloss, 1974). Whereas the endothermic effects in the first temperature interval have been related to the removal of absorbed water within the glauconitic grains, the second temperature interval is related to the loss of hydroxyl water and gradual decomposition of the mineral. The exothermic effect at the temperature interval between 270 °C–410 °C (peak around 360 °C) is related to the oxidation of structural iron (Fe^{2+}) and its transition to a trivalent state (Fe^{3+}).

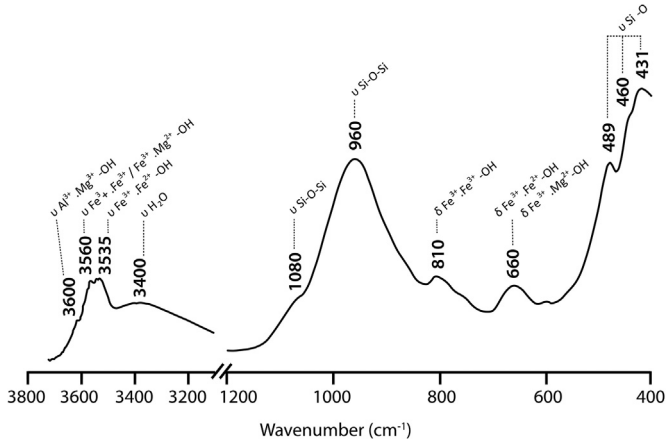

Fig. 3. Infrared spectra (Kbr Transmission) of the pellet shaped, green mineral found in the Blombos Cave sediments, identified as glauconite.

Following the removal of structural water, haematite (Fe_2O_3) begins to form in the temperature interval between c. 700 and 970 °C (Heller-Kallai and Rozenson, 1980; Pavlyukevich et al., 2005). Continuous heating above 1000 °C results in the partial formation of wüstite (FeO), magnetite (Fe^3O^4) and subsequent formation of compositionally diverse magnesium alumoferrites, faylite and cristobalite (Pavlyukevich et al., 2005; Dooley, 2006).

The thermal alteration of glauconitic minerals leads to specific changes in their FTIR spectra. These alterations involve: (1) dehydroxylation, which is identifiable as broadening and loss of absorption bands related to the stretching and bending vibrations of the hydroxyl groups when heated to above 600 °C (e.g. υ 3560 cm^{-1} and 3535 cm^{-1}) (Marel et al., 1976); and (2) a collapse of the mineral structure, most often characterized by a gradual shift of the strong Si–O absorption band at 960 cm^{-1} to higher wavenumbers, when the mineral is heated to 600 °C (Affonso and Pernicka, 2001).

3. Material and methods

3.1. Analytical scope and objectives

Previous FTIR analyses of burnt archaeological sediments using bulk samples have often been limited in terms of spatial and thermal resolution (Berna et al., 2007; Eliyahu-Behar et al., 2012; Friesem et al., 2014a; Forget et al., 2015). By low spatial resolution, we refer to work based on non-oriented, bulk samples macroscopically collected in the field, without a precise geo-referencing or orientation. To improve the spatial resolution of our study, we combine FTIR analyses on bulk samples (low-resolution sampling), with micro-FTIR measurements (e.g. Berna et al., 2012; Goldberg et al., 2012; Shahack-Gross et al., 2014; Villagran et al., 2017) conducted directly on glauconitic mineral grains within polished thin sections (high-resolution sampling).

By low thermal resolution, we refer to the relatively low amounts of temperature thresholds that can reliably be inferred from a typical FTIR analysis. In many cases, e.g. for clay minerals, clear molecular alteration only occurs when temperatures reach between 450 °C and 600 °C (Berna et al., 2007; Weiner, 2010; Friesem et al., 2014a). Furthermore, the rapid dehydroxylation process in clay minerals often only allows for a binary heat classification, i.e. below and above a specific temperature threshold (Forget et al., 2015; Stevenson and Gurnick, 2016). To improve the thermal resolution of this study, we include a complementary, glauconite-based temperature proxy: thin-section grain colour. While the glauconite in the Blombos Cave bedrock occurs as unaltered, dark or pale green grains in thin sections (PPL, Fig. 2b), many of the grains observed in the stratified archaeological deposits appear homogeneously yellow, red and black (Fig. 2c). Their intact grain morphology, homogenous colour alteration and original micro-contextual association with combustion residues, all suggest that they have been optically altered due to heat exposure, rather than to natural weathering.

To investigate the optical and molecular alteration of glauconite we first conducted controlled heating experiments on geological samples collected from the Blombos Cave bedrock. The control samples allow us to measure, with FTIR, micro-FTIR and petrographic microscopy, any structural changes in the glauconite mineral following exposure to known temperature intervals. These reference measurements were then compared and used to quantitatively classify by temperature the infrared and optical measurements conducted on the archaeological thin section samples.

3.2. Material and sample preparation

To study the local glauconitic minerals in their natural, unaltered state, we first collected a fresh rock sample from the cave roof (BBC-13-21). To study any potential taphonomic effects on the bedrock, we also collected a fragmented bedrock sample (roofspall) that was recovered from an unburnt MSA layer (unit CJ) during excavation (BBC-13-22). From both the fresh and the weathered bedrock blocks, we extracted pure glauconite grains by manually separating them from the calcareous matrix, before dividing them into 14 bulk sub-samples (BBC-G-1 to 15) containing 60–70 individual glauconite grains each (Table 1). From the lower part of the south section of Blombos Cave, in archaeo-stratigraphic unit ClBh2 (Phase M3, dated to 94–97 ka) an oriented micromorphological block sample (BBC-13-14) was collected from a >10 cm thick combustion feature (Fig. 1c). A total of 6 geological control samples and 3 archaeological samples were collected (Table 1), resulting in the production of 9 thin sections, following protocols described in Miller et al. (2016). All thin sections were left without a cover slip to facilitate micro-FTIR measurement.

3.3. Laboratory-based heating experiments

To test whether different FTIR methods (bench vs. micro-FTIR) conducted on different sample types (bulk vs. thin sections) would produce different results, a prearranged experimental design was followed (Fig. 4). Bulk samples and non-impregnated block samples of the Blombos Cave bedrock were first heated in porcelain crucibles – each to a 100° (bulk) or 200° (block) temperature interval, and up to 800 °C, in a muffle furnace (Carbolite ELF 11/6B/E301). The samples were gradually heated (95 °C/min) and kept at the same interval temperature for 2 h, before being cooled down to ambient temperature. The bulk samples were then used for bench-FTIR analysis, while the heated block samples were impregnated and finally made into reference thin sections and subjected to micro-FTIR measurements.

3.4. Bench fourier transform infrared spectrometry (FTIR)

FTIR spectroscopy was conducted on 15 glauconite bulk samples using a Cary 660 FTIR spectrometer (Agilent Technologies). The bulk samples were analysed, both in transmission mode (15 spectra, 64 scans at 4 cm^{-1} resolution), and in attenuated total reflectance (ATR) mode (15 spectra, 64 scans at 4 cm^{-1}) following protocols applied in) (see Table 1 for details). While the bench FTIR ATR spectra are published in this paper (Fig. 5), peak value

Table 1
Overview of samples and measurement techniques.

Sample Type	Sample overview					FTIR measurements					Optical documentation/measurements			
	Sample ID	Sample state	Sampled from	Temp.	Duration	Total # of FTIR Spectra	FTIR KbR[a]	FTIR ATR[b]	m-FTIR ATR GE[c]	m-FTIR transmission[d]	Micro-graphs	Colourimetric measurements	High-res scan	Geo-referencing
Control bulk samples (n = 14)	BBC-G-1	Loose	Roof bedrock (fresh)	25 °C	–	2	1	1	–	–	X[e]	–	–	–
	BBC-G-2	Loose	Roof bedrock (fresh)	100 °C	2 h	2	1	1	–	–	X[e]	–	–	–
	BBC-G-3	Loose	Roof bedrock (fresh)	200 °C	2 h	2	1	1	–	–	X[e]	–	–	–
	BBC-G-4	Loose	Roof bedrock (fresh)	300 °C	2 h	2	1	1	–	–	X[e]	–	–	–
	BBC-G-5-1	Loose	Roof bedrock (fresh)	400 °C	2 h	2	1	1	–	–	X[e]	–	–	–
	BBC-G-5-2	Loose	Roof bedrock (fresh)	400 °C	2 h	2	1	1	–	–	X[e]	–	–	–
	BBC-G-5-3	Loose	Roof bedrock (fresh)	400 °C	2 h	2	1	1	–	–	X[e]	–	–	–
	BBC-G-6-1	Loose	Roof bedrock (fresh)	500 °C	2 h	2	1	1	–	–	X[e]	–	–	–
	BBC-G-6-2	Loose	Roof bedrock (fresh)	500 °C	2 h	2	1	1	–	–	X[e]	–	–	–
	BBC-G-6-3	Loose	Roof bedrock (fresh)	500 °C	2 h	2	1	1	–	–	X[e]	–	–	–
	BBC-G-7-1	Loose	Roof bedrock (fresh)	600 °C	2 h	2	1	1	–	–	X[e]	–	–	–
	BBC-G-7-2	Loose	Roof bedrock (fresh)	600 °C	2 h	2	1	1	–	–	X[e]	–	–	–
	BBC-G-7-3	Loose	Roof bedrock (fresh)	600 °C	2 h	2	1	1	–	–	X[e]	–	–	–
	BBC-G-8	Loose	Roof bedrock (fresh)	700 °C	2 h	2	1	1	–	–	X[e]	–	–	–
	BBC-G-9	Loose	Roof bedrock (fresh)	800 °C	2 h	2	1	1	–	–	X[e]	–	–	–
Control thin sections (n = 6)	BBC-13-21	Thin section	Roof bedrock (fresh)	25 °C	–	24	–		12	12	X[f]	34	X	X
	BBC-13-22	Thin section	Weathered bedrock[g]	25 °C	–	22	–		11	11	X[f]	39	X	X
	BBC-13-21-200	Thin section	Roof bedrock (fresh)	200 °C	2 h	22	–		11	11	X[f]	35	X	X
	BBC-13-21-400	Thin section	Roof bedrock (fresh)	400 °C	2 h	24	–		12	12	X[f]	43	X	X
	BBC-13-21-600	Thin section	Roof bedrock (fresh)	600 °C	2 h	26	–		13	13	X[f]	38	X	X
	BBC-13-21-800	Thin section	Roof bedrock (fresh)	800 °C	2 h	20	–		10	10	X[f]	31	X	X
Archaeological thin section (n = 3)	BBC-13-14 (a-b-c)	Thin section	G6d, CIB - CK/CL	h	h	406	–		203	203	X[f]	203	X	X

[a] 64 scans, 4 cm-1 resolution, 4400–400 cm-1 scan range.
[b] 64 scans, 4 cm-1 resolution, 4400–400 cm-1 scan range.
[c] 128 scans, 4 cm-1 resolution, 4400–400 cm-1 scan range.
[d] 128 scans, 2 cm-1 resolution, 4000–3000 cm-1 scan range.
[e] Taken of smear mounts with reflective/Oblique light.
[f] Taken on thin sections with plane Polarized Light (PPL) and Cross-Polarized light (XPL).
[g] Bedrock roof spall found within the archaeological sediments, unit CJ in the MSA sequence.
[h] Unknown heat exposure and duration.

comparisons between transmission and ATR are provided in Table 2 (for full peak database see Appendix B). 163 raw spectra files (CSV-format) of measurements conducted on the control samples are provided in Appendix C.

3.5. Microscopic Fourier transform infrared spectrometry (micro-FTIR)

Microscopic Fourier transform infrared spectrometry (micro-FTIR) was carried out using a Cary 610 FTIR microscope attached to a Cary 660 bench (Agilent Technologies). Seven thin sections were analysed, resulting in 544 individual measurements (see Table 1 for details). The measurements were taken both in transmission mode (128 scans at 4 cm^{-1} resolutions) and in attenuated total reflectance (ATR) mode (128 scans at 2 cm^{-1} resolution) using a germanium crystal (Ge-ATR) objective. The micro-FTIR transmission measurements enabled us to define the absorption peaks in the higher frequency OH-stretching region (3700-3100 cm^{-1}), whereas the micro-FTIR GE-ATR measurements provided high-resolution spectra of the lower frequencies (1200-400 cm^{-1}). All FTIR and micro-FTIR spectra (n = 574) were processed and analysed using the Agilent Resolutions Pro software.

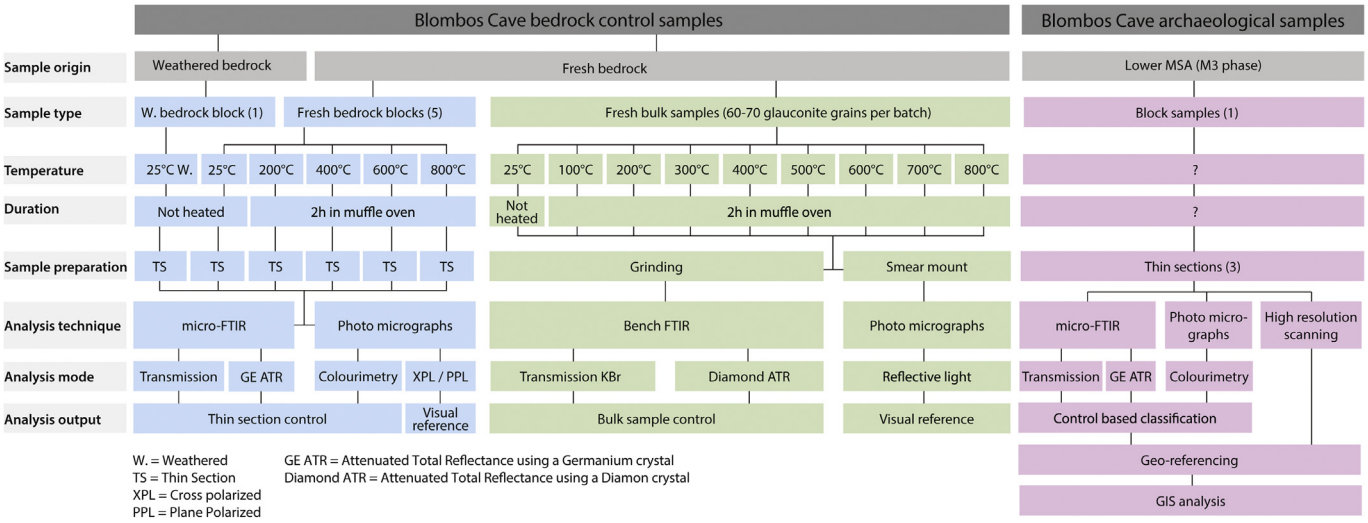

Fig. 4. Flowchart showing: (a) the design of the laboratory heating experiments of bedrock control samples (blue = block samples, green = bulk samples); (b) the workflow for analysing the archaeological block samples (pink) (see Table 1 for an overview of samples). (For interpretation of the references to colour in this figure legend, the reader is referred to the web version of this article.)

3.6. Petrographic microscopy and colourimetry

Colours in thin sections is a function of the combined thickness of glass, resin and material. Thus, the use of different types of glass and inconsistency during thin section production may result in different colour values. To improve the internal accuracy of the colour measurements, and to ensure image-capturing consistency for the optical analysis of glauconite grains in thin sections, a colourimetric protocol was established (Table 3).

All thin sections were documented using a Zeiss Axio Imager petrographic microscope (25x-200x), and conventional thin section micrographs were taken with a Zeiss Axiocam MRc 8 (1.4 megapixels), in both plane-polarized light (PPL) and cross-polarized light (XPL). For the image-based colourimetric analysis, photo-micrographs (200x magnification, PPL) were taken of the glauconite grains, both in the thin section control samples (n = 220) and in the archaeological samples (n = 203) (Fig. 5a). Each colour measurement represents the average colour value of a sampled area (50 × 50 pixels) of the grain surface in thin section (Fig. 5b). The average colour area was then converted into numerical values within a 3-dimensional colour space, CIE L*a*b* (CIELAB) (Fig. 5c, see also supplementary fig. A.2), before being subjected to discriminant analyses (for full database see Appendix B).

3.7. Geo-referencing of archaeological thin sections and spatial interpolation of data

The archaeological thin sections, subjected to micro-FTIR and colourimetric analyses, were all scanned in high resolution (4000 DPI), with a modified Nikon Coolscan LS-8000 ED Film Scanner. The high-resolution scans were imported into a GIS application (ArcGIS ArcMap 10.3) and geo-referenced within the 3D coordinate system of the archaeological excavation. In the GIS application, using the geo-referenced thin section scans as visual guidance, all micro-FTIR and colourimetric measurements were digitised as point data. The spatial distribution of these points, combined with the colourimetric and FTIR-based assessment of temperature exposure, allowed us to interpolate point temperature data across the sampled area, using *Inverse Distance Weighted* (IDW) interpolation techniques (see Appendix A for details).

4. Results

4.1. Fourier transform infrared spectrometry (FTIR) of glauconite bulk control samples

The ATR spectra from FTIR measurements conducted on the glauconite bulk control samples (BBC-G-1 to 15) are shown in Fig. 6 (see figure legend for details and Table 2 for band assignments). When glauconite is heated to more than 500 °C, we observe several peak shifts and peak losses, the most noticeable being:

- A loss of the hydroxyl groups in the 3530-60 cm^1 region:
  - o 3560-3565 cm^{-1} (υ Fe3+.Fe^{3+}/Fe^{3+}.Mg^{2+} −OH)
  - o 3535-3543 cm^{-1} (υ Fe^{3+}.Fe^{2+} −OH).
- A shift in the strong υ Si−O−Si absorption peak at 960 cm^{-1} towards 988 cm^{-1}
- A loss of the 810 cm^1 peak (δ Fe^{3+}.Fe^{3+} −OH)
- A very weak absorption peak evolves at 680 cm^1 (δ Fe^{3+}.Fe^{2+}/Fe^{3+}.Mg^{2+} −OH)
- A loss of the 484 cm^{-1} peak (δ Si−O)

4.2. Microscopic Fourier transform infrared spectrometry (micro-FTIR) of glauconite grains in thin section control samples

Representative micro-FTIR spectra (transmission and GE ATR) from each control sample are shown in Fig. 7 (see figure legend for details, Table 2 for band assignments and supplementary Table B 1 for full peak database). The micro-FTIR spectra of glauconite grains in thin section are very similar to those produced by the bench FTIR. Some of the peaks, however, appear to have a slight offset. The strong υ Si−O−Si absorption at 960 cm^{-1} obtained from the bench FTIR ATR, for example, are consistently found around 940 cm^1 in the micro-FTIR GE ATR spectra. We regard this systematic shift, to a lower wave number, as a consequence of different measuring methods, and it should not be confused with any of the heat-induced peak shifts. We note that most of the heat-induced changes observed in the bench FTIR spectra of glauconite are also present in the micro-FTIR spectra:

Fig. 5. Image-based, colourimetric recording of glauconite grains in thin section: (a) Photomicrographs of unheated and heated glauconite grains (PPL, 200x). The White rectangle is indicating the 50 × 50 pixel sampled surface; (b) Close-up of sampled surface; (c) Averaged colour of sampled surface area. The white numbers represent the CIELAB colour value of the averaged surface. (For interpretation of the references to colour in this figure legend, the reader is referred to the web version of this article.)

- A loss of hydroxyl groups in the 3530-60 cm^1 region:
  - o 3559-3563 cm^{-1} (υ Fe3+.Fe^{3+}/Fe^{3+}.Mg^{2+} –OH)
  - o 3535-3543 cm^{-1} (υ Fe^{3+}.Fe^{2+} –OH).
- A loss of the weak 807–813 cm^1 peak (δ Fe^{3+}.Fe^{3+} –OH)
- A very weak absorption peak disappears at 658–660 cm^1 (less ordered δ Fe^{3+}.Fe^{2+}/Fe^{3+}.Mg^{2+} –OH)
- A very weak absorption peak evolves at 685 cm^1 (δ Fe^{3+}.Fe^{2+}/Fe^{3+}.Mg^{2+} –OH)

If we compare bench FTIR (ATR) measurements with the micro-FTIR spectra of heated glauconite, we note that the loss of the 484 cm^{-1} peak (δ Si–O) can no longer be discerned. Furthermore, we see that the prominent shift of the υ Si–O–Si absorption peak in the bench FTIR spectra is no longer significant in the micro-FTIR spectra (Table A.2). Consequently, and in contrast to the bench-FTIR spectra of bulk samples, we do not regard the Si–O–Si peak alteration in micro-FTIR spectra to be a reliable marker for heat-exposed glauconite grains in thin section.

The most consistent heat-induced, molecular changes that we can observe in the FTIR-spectra of glauconite are the presence and absence of the 3532 cm^{-1} peak (cf. Villagran et al., 2017); here defined as P1) (υ Fe^{3+}.Fe^{2+} –OH) and the 810 ^{cm1} peak (here defined as P2) (δ Fe^{3+}.Fe^{3+} –OH) (Fig. 8). By using the normalized height of P1 and P2 in a bi-plot, we can see a clear correlation between the absence and presence of these two peaks and their relation to temperatures above and below 600 °C (Fig. 9). Since the P2 measurements fluctuate more than P1, we chose to focus on the presence and absence of P2, as indicative of heat exposure below or above 600 °C when assessing the micro-FTIR measurements of glauconite on the archaeological thin sections.

4.3. Colourimetric analysis of glauconite grains in thin section control samples

Fig. 10a shows a principle component analysis (PCA) of the CIELAB colour values of 221 measured glauconite grains in the thin section control samples, where the multivariate means of all measurements are plotted in the two dimensions that best separate the temperature groups (supplementary Table B 2). The PCA plot show that the glauconite grains in the heated control samples alter their colour systematically and form distinct colour clusters in strong correlation to the temperatures to which they were heated.

The PCA plot of unheated (green dot) and weathered glauconite (green triangle) grains are similar to that of grains heated to 200 °C (dark green dot). The colour of these three groups corresponds to various nuances of green (mean LAB value = 42, −2.5, 10) and cannot be quantitatively distinguished. The multivariate means of glauconite heated to 400 °C (orange dot), 600 °C (dark red dot) and 800 °C (black dot) form three distinct clusters, as a clear function of increasing temperatures. Their colour values correspond to pale yellow/orange at 400 °C (mean LAB value: 43, 4, 16), dark red at 600 °C (mean LAB value: 24, 7, 8.5) and dark grey or black at 800 °C (mean LAB value: 22, 3, 2.5). The unheated, weathered and moderately heated glauconite grains (heated to below 600 °C) are significantly lighter (L+) than those heated to above 600 °C (L-). Furthermore, unheated or moderately heated glauconite grains (25–200 °C) are considerably greener (A-) than those heated to 400 °C, which contains more yellow (B+). Finally, glauconite grains heated to 600 °C hold more red values (A+) than grains heated to 800 °C, which are bluer (-b) and considerably darker (-L).

In a canonical plot for a linear discriminant analysis, we can quantitatively distinguish between the following colour-based temperature classes: 25–200 °C, 400 °C, 600 °C and 800 °C (coloured circles in Fig. 10b, supplementary Table 2). The internal misclassification rate for our control data set in the canonical plot (predicted vs. actual temperature class) is 7.6% (17 of 220). The misclassified grains exclusively belong to either the 400 °C or the 600 °C temperature class.

4.4. Infrared and colourimetric classification of glauconite grains in archaeological thin sections

All colour measurements (n = 203) conducted on the archaeological thin sections of a combustion feature in the lower part of the MSA sequence of Blombos Cave (cf. Fig. 11 for exact sampling location), were converted to 3-dimensional CIELAB values, and subsequently compared to the multivariate mean colour values of the glauconite grains in the heated control samples, using a

Table 2
Comparison and peak assignment of FTIR and micro-FTIR spectra of Blombos Cave glauconite with published glauconite spectra.

Chukanov 2014	Odin et al., 1988		Unheated glauconite minerals from Blombos Cave bedrock			
Bulk	Bulk		Bench FTIR on bulk samples		micro-FTIR on thin sections	
Transmission	Transmission	Assignment	Transmission	Diamond ATR	Transmission	Germanium ATR
3645sh	–	–				
3600sh	3604[a]	υ Al^{3+}.Mg^{3+} –OH	–	–	–	–
3560	3560	υ Fe3+.Fe^{3+}/Fe^{3+}.Mg^{2+} –OH	3560	3560	3559	–
3540sh	3534–3544	υ Fe^{3+}.Fe^{2+} –OH	3535	3535	3533	–
	3440br	υ H_2O (variable)	3432br	3396br	3401br	–
3365	–	–	–	–	–	–
3240sh	–	–	–	–	–	–
1630w	–	–	–	–	–	–
1120sh	1070–1080	υ Si–O–Si (Tetrahedral sheet, variable)	1120sh	–	–	–
1029s	990–1025	υ Si–O–Si (Tetrahedral sheet)	984s	963s	–	945
995sh	–	–	–	–	–	–
877	880[a]	δ Al^{3}+.Fe^{2+} –OH	–	–	–	–
	835[a]	δ Al^{3}+.Mg^{2+} –OH	–	–	–	–
819w	815–818	δ Fe^{3}+.Fe^{3+} –OH	812w	810w	–	810w
	763w[a]	–	–	–	–	–
677w	679	δ Fe^{3+}.Fe^{2+}/Fe3+.Mg2+ –OH	672	666	–	669
	660[a]	-δ Fe^{3+}.Fe^{2+}/Fe^{3+}.Mg^{2+} –OH (less ordered)	–	–	–	658sh
489s	495–489	δ Si–O (variable)	491s	485s	–	489
460s	452	δ Si–O	451s	–	–	–
431sh.	434	δ Si–O (variable)	431sh	425	–	–

s: strong band.
br: broad band.
w: weak band.
sh: shoulder
υ: stretching vibration modes.
δ: bending vibration modes.
[a] sometimes lacking.

Table 3
Protocol for colourimetric analysis of glauconite grains in thin sections.

1. Glauconite grain selection criteria (in thin section)
1.1. The grain must have a clear and unbroken boundary (not be heavily weathered or cracked)
1.2. The grain must have a homogenously coloured surface (not be heavily overprinted with other material or substances)
1.3. The grain must be larger than 50μ (enabling m-FTIR ATR measurement).
1.4. The grain must be in an area of the thin section that has a correct thickness of 30μ.
1.5. The selected grains are distributed evenly across the thin sections.
2. Microscope settings and photo-micrograph calibration
2.1. Microphotographs of grain surfaces were taken at 200x magnification (20 × 10)
2.2. All automatic photo capturing settings were turned off and manually adjusted to ensure that all images had a consistent white balance, exposure, and contrast enhancement.
2.3. The colour profile of the images was not calibrated to true colour, but may be considered internally consistent and valid for this case study.
3. Image editing and surface area selection criteria
3.1. All photo microphotographs were opened in Adobe Photoshop CS 6 and a sampled surfaces area from the mid part of the glauconite grain was selected (ca. 50 × 50 pixels) (Fig. 3a).
3.2. The average grain colour within the cropped area was then calculated using the 'Average Tool' (Fig. 3b)
4. Colour quantification and statistical classification
4.1. The averaged grain colour value was extracted using the 'Colour Sampler Tool' and numerically quantified within the 3-dimensional colour space: CIE L*a*b* (CIELAB) (Fig. 3c).
4.2. The CIE L*a*b* colour data was coupled with the m-FTIR database and all subsequent multivariate analysis and classification were then conducted in JMP 11 software.

canonical plot (Fig. 10 b, supplementary Table B 3).

When compared to the micro-FTIR temperature classification (below or above 600 °C), the colour-based misclassification rate for the archaeological samples is 6.7%. That is, 14 of 203 measurements on the archaeological thin sections were classified differently by the two respective methods (colour vs. micro-FTIR). In Fig. 10b we observe that most of the differently classified grains (n = 14) fall outside the 50% mean colour value range of any of the control group. These outlier measurements are in general lighter (L+) and redder (A+) than those measured at 400 °C or 600 °C in the thin section control samples. The lighter and redder colour suggest that they fall into a theoretical 500 °C class. At least 13 of the outlier colour measurements were originally classified to the 600 °C class, but considering their micro-FTIR spectra they were likely not heated to this degree. We therefore manually reclassified these 13 points, back to the 400 °C temperature class (orange star on

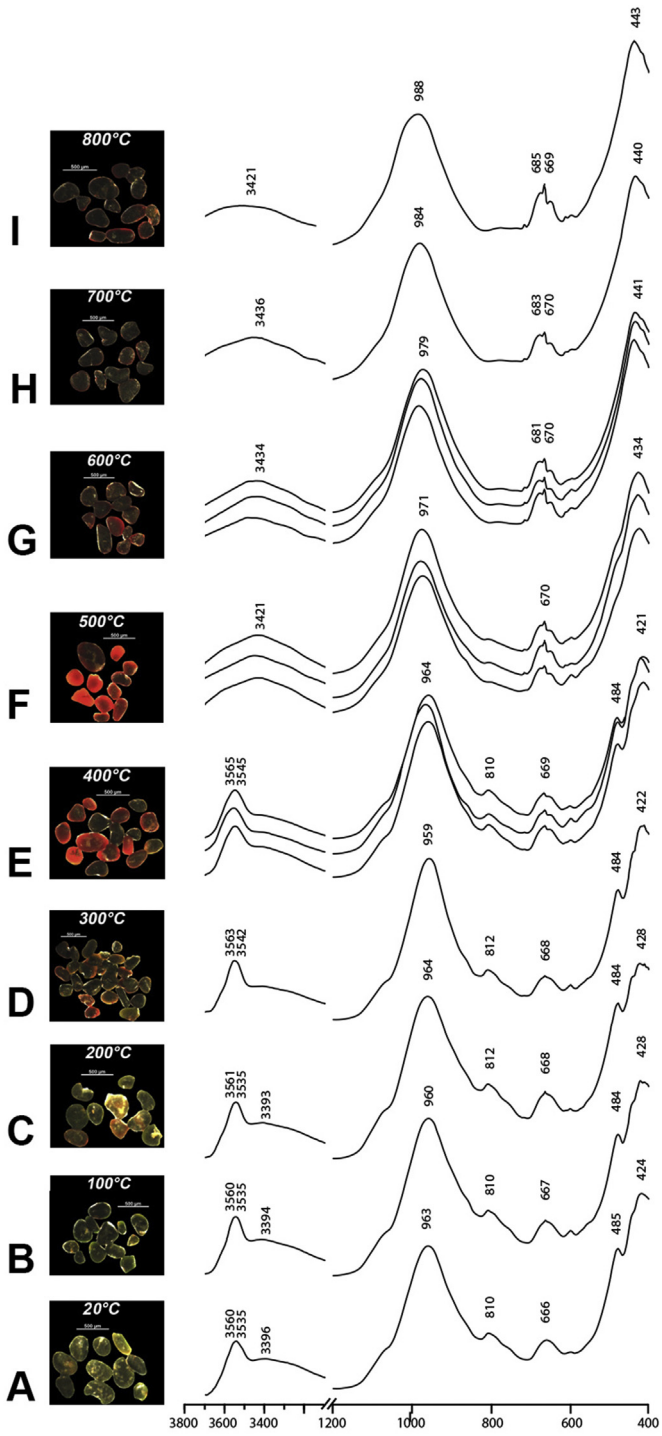

Fig. 6. Photomicrographs (reflective light) and infrared spectra (ATR mode, 64 scans at 4 cm−1) of glauconite bulk samples extracted from the Blombos Cave bedrock and heated for 2 h in an oven to various temperatures. (a–c) Non-heated or moderately heated, green glauconite grains. No alteration of infrared spectra; (d–e) Moderately heated, orange (300 °C) and red (400 °C) glauconite grains. No alteration of infrared spectra; (f–i) Heated glauconite grains that turn bright red at 500 °C, dark red at 600 °C and black at 700 °C and 800 °C. Alteration of infrared spectra includes: loss of hydroxyl groups in the 3530-60 cm-1 region and hydroxyl groups that are in coordination with Fe3+ and Mg cations at 810 cm-1 and 660 cm-1. Also, the strong υ Si–O–Si absorption peak at 960 cm-1 shifts to 971-988 cm-1 and the 484 cm1 (δ Si–O) disappears. (For interpretation of the references to colour in this figure legend, the reader is referred to the web version of this article.)

Fig. 10c). One colour measurement was originally classified to the 400 °C class, but considering its micro-FTIR spectrum, it was most likely heated to above 600 °C. This single measurement we manually reclassified to the 600 °C temperature class (red star on Fig. 10c).

4.5. Temperature distribution models

4.5.1. Micro-FTIR based temperature model

Fig. 12a shows the spatial distribution of individual glauconite grains by their micro-FTIR based temperature classification (Fig. 10b). The glauconite grains exposed to temperatures below 400° (green dots) are primarily found in the sandy matrix (calcareous and quartz-rich sand) below and above the combustion feature, while the heavily burnt grains are found in the middle. When the value of these point measurements are interpolated (IDW) into a temperature distribution map, this pattern becomes more clear Fig. 12b.

4.5.2. Colour based temperature model

Fig. 12c shows the spatial distribution of individual glauconite grains by their CIELAB colour-based temperature classification (Fig. 10c). Again, we note that the glauconite grains classified to the 20–200° temperature groups (green dots) are primarily found in the bottom part of the sandy matrix below and above the white, ash-rich areas. Most of the grains exposed to temperatures around 400° (yellow dots) are found at the very base of ashy deposits. The glauconite grains exposed to temperatures between 600° and 800° (red and black dots) are almost exclusively found in the centre (cf. IDW model in Fig. 12d).

4.5.3. Colour based, micro-FTIR corrected, temperature model

We note that the colour-based classification produced a temperature model that is consistent with the micro-FTIR based model (Fig. 12b), yet some minor discrepancies can be observed (primarily glauconite grains classified by their colour as heated to above 600°, but by their micro-FTIR spectra to less than 600°). Fig. 12e shows the spatial distribution of glauconite grains by micro-FTIR corrected CIELAB colour-based temperature classification (Fig. 10c). The overall difference between the original colour-based model (Fig. 12d) and the micro-FTIR corrected model (Fig. 12f) is minimal.

5. Discussion

5.1. Heat-induced optical and structural alteration of glauconitic minerals

The results of the controlled lab experiments and colourmetric analysis show that glauconitic minerals in the Blombos Cave thin sections undergo a gradual and systematic colour change when exposed to increasing temperatures. The unheated, green glauconite grains turn yellow when temperatures reach higher than c. 300–400 °C, bright red at 500 °C, dark red at 600 °C and red-brown or black (opaque) at 700–800 °C. At the same time, when temperatures reach higher than c. 600 °C, our FTIR and micro-FTIR measurements show that the glauconite grains also undergo clear structural changes; namely the loss of hydroxyl groups in the 3530-60 cm^{-1} region and hydroxyl groups that are in coordination with Fe^{3+} and Mg cations at 810 cm^{-1} and 660 cm^{-1}.

Based on the thermal properties of glauconite (Fig. 13) we relate the red and yellow, heat-induced colour alteration to the gradual oxidation of iron that occurs between 250 °C and 450 °C and the darker red and black coloured grains to the gradual transformation of glauconite to haematite (<600 °C). We relate the structural

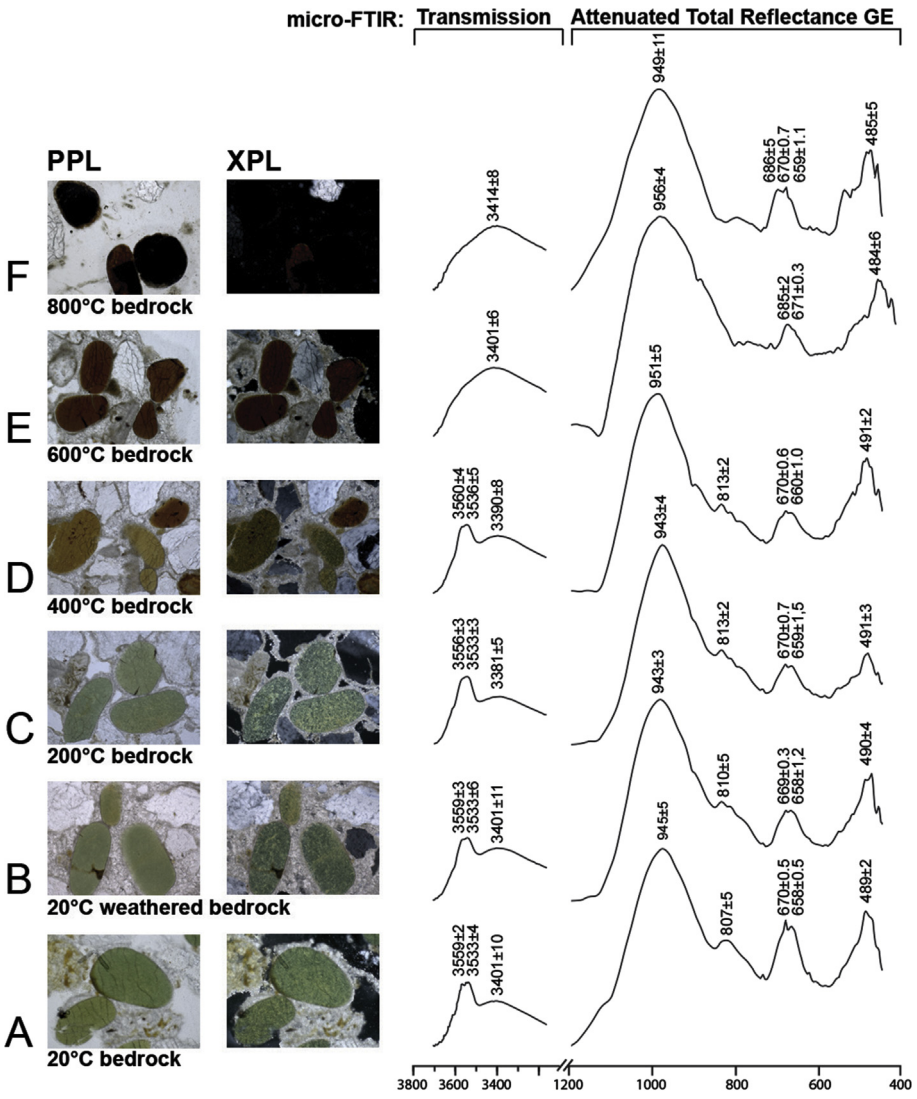

Fig. 7. Photomicrographs (PPL and XPL, 200x) and a representative micro-FTIR spectra of glauconite grains in thin sections made from blocks of Blombos Cave bedrock and heated for 2 h in an oven to various temperatures (10–12 measurements per temperature interval, see Table B.1). High-frequency regions were measured by m-FTIR transmission (128 scans, 2 cm-1 resolution) and for the lower regions, micro-FTIR GE ATR was applied (128 scans at 4 cm−1). Non-heated and moderately heated glauconite grains in thin section are green in PPL and have the following absorption peaks in transmission mode: 3559 cm-1 (υ Fe^{3+}.Fe^{3+}/Fe^{3+}.Mg^{2+} –OH), 3533cm-1 (υ Fe^{3+}.Fe^{2+} –OH) and broad 3400 cm1 (υ H2O). In GE ATR the following peaks are present: a strong 943–945 cm1 (υ Si–O–Si), a weak 807–810cm1 (δ Fe^{3+}.Fe^{3+} –OH), a weak doublet at 658 and 670 cm1 (δ Fe^{3+}.Fe^{2+}/Fe^{3+}.Mg^{2+} –OH), and a sharp 490 cm1 (δ Si–O); (b) Non-heated, weathered glauconite grains in thin section are pale-green and show the same absorption peak as fresh glauconite from the bedrock; (c–d) The FTIR spectra of glauconite grains in thin sections heated to 200 °C and 400 °C show little difference from spectra of un-heated glauconite. Optically, glauconite heated to 400 °C undergo a colour change, from pale green to yellow and orange; (e–f) At 600 °C and 800 °C, the spectra of glauconite in thin sections show clear alterations; a loss of hydroxyl groups in the 3530-60 cm-1 region and hydroxyl groups that are in coordination with Fe^{3+} and Mg cations at 810 cm-1 and 660-670 cm-1. Unlike the bench FTIR spectra, we see in the m-FTIR spectra that the strong υ Si–O–Si absorption peak at 940-950 cm-1 do not show a clear shift towards higher frequencies, and the 490 cm1 (δ Si–O) peak do not disappear at higher temperatures. (For interpretation of the references to colour in this figure legend, the reader is referred to the web version of this article.)

breakdown of glauconite minerals, indicated by peak shifts and losses in both bench-FTIR and micro-FTIR spectra of grains heated to above 600 °C, to the effects of dehydroxylation and gradual haematite formation.

5.2. Accuracy and reproducibility of colourimetric measurements

The colourimetric selection protocol we established (Table 3) ensured that all colour and capturing settings were kept the same, and we avoided picking grains that were optically altered either due to natural weathering or overprinting of material (cf. supplementary figure A.2), or variation in thin section manufacturing (polishing). Considering the PCA plots of our control samples, we regard our results to have high internal consistency. It should, however, be noted that the thin section production and the colour measuring procedure may vary among different lab setups. The absolute colour values and colour-classification index presented in this paper must therefore be tested and calibrated before being used directly on material from other sites. We nonetheless regard the relative differences in values to be highly indicative of how increasing temperatures alter the colour of glauconitic grains in general.

5.3. Reliability of colourimetric and FTIR-based classification

By applying our colour-based classification scheme (Fig. 10) on

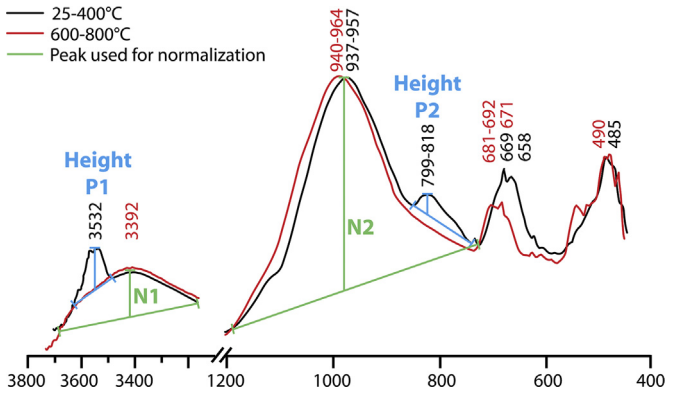

Fig. 8. Comparison of micro-FTIR spectra of glauconite grains in thin sections made from blocks of Blombos Cave bedrock heated to above and below 500 °C. The black spectrum is representative for un-heated glauconite. The red spectrum is representative for glauconite heated to 600 °C and 800 °C. The clearest and most robust difference between these spectra, consistently observed in all control spectra (n = 69) are the presence and absence of the 3532 cm-1 peak (P1) (υ Fe^{3+}.Fe^{2+} –OH) and the weak 810 cm1 peak (P2) (δ Fe^{3+}.Fe^{3+} –OH). Consequently, the normalized heights of P1 and P2 were used as proxies for heat exposure and temperature assessment (below and above 500 °C). The height of P1 was normalized by the height of N1 and the height of P2 was normalized by the height of N2. A biplot of these values is shown in Fig. 9. (For interpretation of the references to colour in this figure legend, the reader is referred to the web version of this article.)

samples of glauconite grains heated to known temperatures, a 6–8% misclassification rate was reached (17 of 220 measurements were wrongly classified). Thus, the colour-based classification system can separate most unheated and lightly heated grains, from those heated to 400 °C, 600 °C and 800 °C. The few misclassified grains are exclusively assigned to either the 400 °C or the 600 °C temperature class and a closer study of these shows that their canonical plot distribution does not correspond well with the colour range of any control group (Fig. 10b). It is thus likely that most of the wrongly classified grains were heated to above 400 °C (yellow/orange) but below 600 °C (dark red). The temperature threshold between 400 °C and 600 °C can, however, be reliably set apart using the FTIR-based temperature classification (Fig. 8). Hence, we conclude that by applying FTIR-informed corrections, the colour-based classification system allows us to correctly categorize 100% of the glauconite grains in the control samples by the temperature range to which they were exposed: 20–200 °C, >400 °C, >600 °C and >800 °C (Fig. 10c).

5.4. Spatial accuracy of temperature interpolation

To assess the general spatial accuracy of our temperature interpolation, we visualized the final heat-intensity model in Fig. 11f, with orthophotographic section photos of the exact location from where the archaeological block sample was originally collected, i.e. the combustion feature in the M3 phase of Blombos Cave. It is clear from Fig. 11g that the interpolated temperature distribution, showing a gradual temperature gradient from top to bottom, conforms to a pattern that one would expect from an *in-situ* combustion feature (March et al., 2014).

5.5. Archaeological implications

5.5.1. The distribution of burnt sediments

At most archaeological sites, examining the distribution of burnt sediments is essential for making statements concerning the location, preservation or function of hearths and combustion features (Berna et al., 2007). In this regard, the plotting of individual,

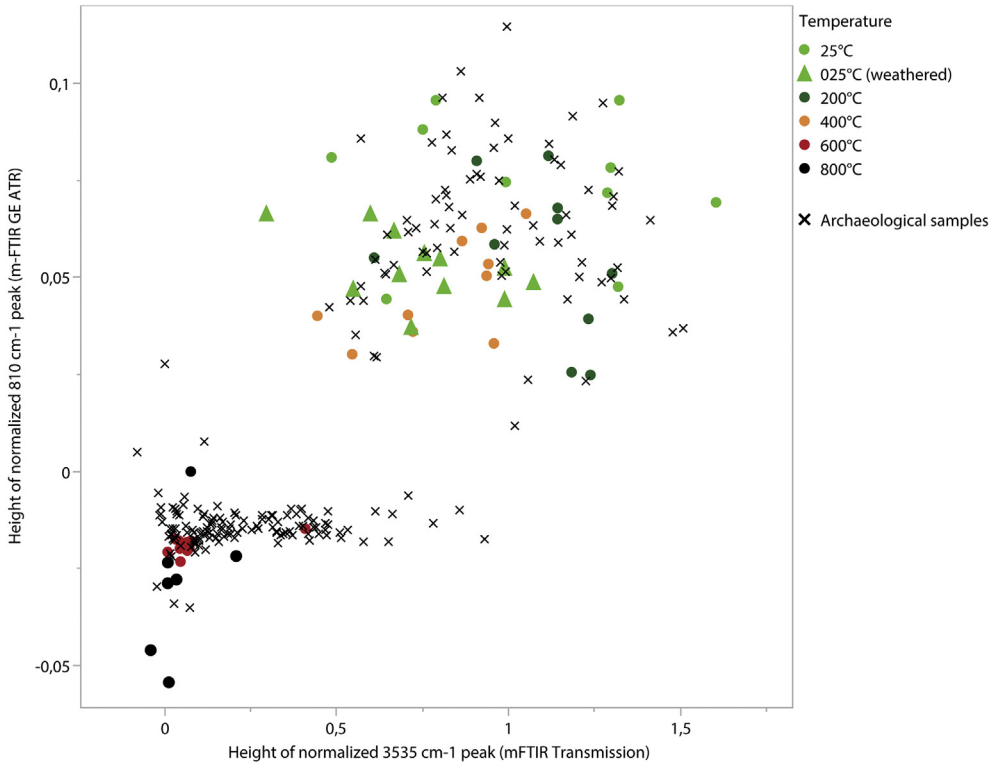

Fig. 9. Biplot of the normalized height of the 3540 cm-1 transmission peak (P1) (υ Fe^{3+}.Fe^{2+} –OH) and normalized height of the 810 cm1 GE ATR peak (P2) (δ Fe^{3+}.Fe^{3+} –OH) (see Table B.1). The control samples are shown as coloured dots by their temperature class and the archaeological measurements as black crosses. Both the known control sample and the archaeological samples shows a clear binary grouping as a function of temperature (below or above 500 °C).

heat-altered glauconite grains in thin sections has some clear advantages. First, compared to other combustion residues, such as ash, glauconite grains do not recrystallize, or dissolve or break down as easily as ash or charcoal. Glauconitic minerals are susceptible to natural weathering under certain conditions; however, the morphology and colour of these grains can be clearly distinguished from those that have been altered by heat alone (McRae, 1972). Consequently, the chemical properties of glauconitic minerals make them a more stable sedimentary component than most other burnt or partially combusted material, from which the presence of past burning events can be reliably inferred. Second, whereas combustion residues most often accumulate in hearths or ash dumps on top of an exposed surface, most heat-altered glauconite grains in Blombos Cave are buried within the deposits beneath the heat source. This protected location likely makes the glauconite grains less susceptible to intentional removal or immediate relocation through surficial processes such as cleaning, sweeping, dumping, trampling or surface-related weathering processes (Fig. 14). Third, the glauconite grains that are found in Blombos Cave are uniformly distributed and occur in abundant quantity throughout the sequence (>100 per 1 cm^2 in thin section).

This large number of grains allows for numerous and independent microscopic observations, which enable the production of high-resolution, spatially referenced datasets that can efficiently discriminate between tiny, irregular and spatially discrete areas of burnt and unburnt deposits. Since the value of each local measurement (single grain value) can be weighed in relation to all surrounding measurements (values of multiple, surrounding grains), we would argue that this type of semi-quantitative, spatio-contextual approach is more robust in its fundamental design (numerous measurements, microscopically geo-referenced) than most studies based on low-resolution bulk-samples (few measurements, non-oriented, macroscopically geo-referenced).

5.5.2. Assessing reworking, internal hearth structure and frequency of burning

Aldeias et al. (2016) document in their experimental study of burnt deposits that the sediments below the centre of a fire source often form a basin-shaped area of rubification due to the heat-induced oxidation of iron-bearing minerals. The size and appearance of this rubified area correspond to the size and temperature of the fire on top of it. The calcareous sediments within Blombos Cave contain few iron components and do not rubify easily. Yet, given the abundance of glauconite grains in the cave sediments, it seems safe to assume that most, if not all, hearths built inside the cave must have caused a permanent molecular alteration to the grains found in the substrate below them, thereby creating a predictable, basin-shaped distribution pattern of heat-altered glauconitic minerals (Fig. 14). While the detailed nature of these heat-induced sediment patterns might be easily overlooked when applying conventional bulk sampling strategies, the single-grain thin-section approach is highly sensitive to microscopic spatial variation within the sampled area. This increased sensitivity permits a more detailed assessment of the spatial integrity of the heat-induced sedimentary distribution patterns; i.e. between deposits burnt *in situ* and burnt deposits that subsequently were reworked or disturbed.

If, for example, rubified sediments below a hearth feature exhibit a basin-shaped morphology with the thicker area of heat alteration being in the centre and the thinner areas towards the side and base, we would interpret this as evidence for *in-situ*, non-disturbed heat-altered deposit (cf. Fig. 8 in Aldeias et al., 2016). If, on the other hand, some of the heat-altered grains below a hearth were to be mechanically removed from their original sub-surface position, e.g. due to trampling, digging or animal burrowing, this would immediately disturb the spatial distribution of the burnt grains within these sediments and a randomized or partially interrupted grain-distribution pattern would result.

Evidence for an intact distribution patterns may indeed be observed in Fig. 12 and Fig. 15. In the lower part of zone A on Fig. 15 for example, we see a heat distribution pattern that is comparable with that of an undisturbed, basin-shaped oxidised zone below a heat source (cf. Fig. 14d).

5.5.3. The morphology of hearths and combustion features

When the spatial distribution of heat-altered sediments is not heavily affected by post-depositional disturbance, the heat-induced distribution patterns within them are primarily governed by the shape, size and structure of the original fire(s) that were lit above them (March et al., 2014). Thus, a study of the spatial distribution of glauconitic minerals in archaeological sediments may also inform us about the overall morphology of the prehistoric feature(s) themselves.

The block sample (BBC-13-14) in our case study was collected in the thickest (10–15 cm) middle part of a basin-shaped combustion feature, which measured c. 60 cm in cross section (Fig. 11a). Macroscopically, the sampled combustion feature seems to qualify as a *basin-shaped hearth,* which in planar view constitutes a circular to oval area, with a depression in its centre (Meignen et al., 2007). Various terminologies have been used to describe such human-made fires: e.g. *pit-hearths* (March et al., 2014), *en cuvette (fr.)* or *contained, intact combustion features* (Mentzer, 2017). These non-formal fires are built directly on top of an unprepared surface, and they normally represent spatially and chronologically confined burning events.

From the distribution of burnt and unburnt glauconite grains at the base of the sampled combustion feature (Fig. 12), we note that the microscopically derived heat distribution pattern in Fig. 12g is spatially and thermally consistent with the macroscopic extent and morphology of white, calcareous material (recrystallized wood ash). This observation strengthens the notion that the distribution of ash and heated glauconite is governed by the same factor: i.e. the size and temperature of the original hearth(s). Yet, while the general morphology of the sampled combustion feature and surrounding strata is indicative of a pit-hearth, the basin-shaped oxidised zone below it could also have been produced by a flat hearth (Aldeias et al., 2016). Therefore, the spatial distribution of glauconitic grains cannot alone differentiate between flat and pit-hearths, and further micromorphological investigation is needed to distinguish effectively between the two fire types.

A discussion concerning the morphology, internal structure and mode of accumulation within a clearly discernible combustion feature, may seem superfluous. However, several archaeological and experimental studies have demonstrated that the physical arrangement of burnt deposits does not necessarily reflect the actual location, nature or dimension of the original fire structure; this can be a result of highly variable, context-specific fire conditions that are difficult to model (Mallol et al., 2007; Bentsen, 2012; March et al., 2014) or it can be due to mechanical reworking and chemical alteration of ash and charcoal over time (Weiner, 2010). We would thus argue that a microscopic investigation of both combustion residues (Mentzer, 2012) and surrounding heat-altered sediments (Canti and Linford, 2000; Berna et al., 2007) offers a more powerful approach to evaluating the general morphology and internal structure of prehistoric hearths and combustion features.

5.5.4. Burning frequency and intensity (temperature)

Due to the thermal characteristics of glauconitic minerals, their degree of alteration may be indicative of burning temperature (directly) and burning frequency (indirectly): two variables that often are linked to the deliberate choices made before and during

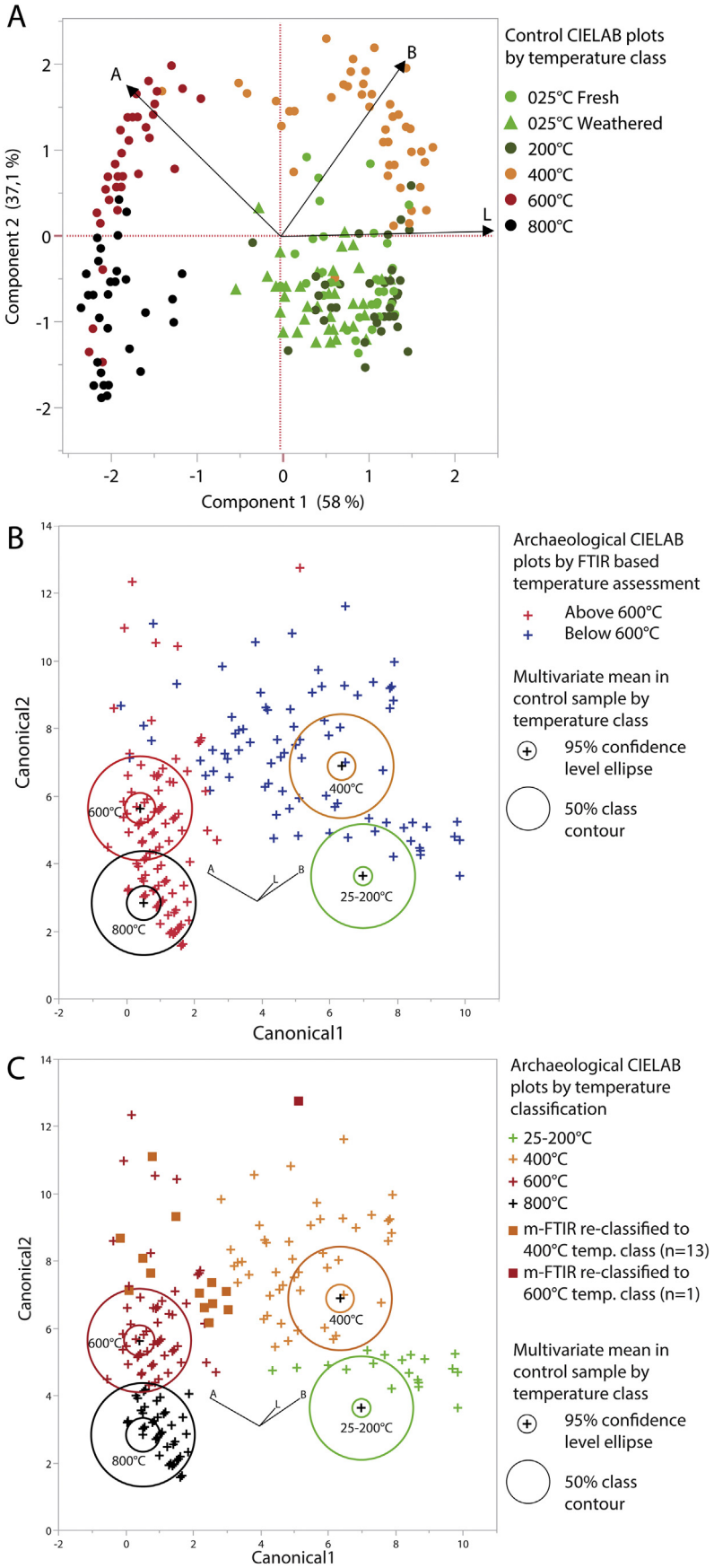
A
Component 2 (37,1 %)
Component 1 (58 %)
A
B
L
Control CIELAB plots by temperature class
025°C Fresh
025°C Weathered
200°C
400°C
600°C
800°C
B
Canonical2
Canonical1
600°C
400°C
800°C
25-200°C
Archaeological CIELAB plots by FTIR based temperature assessment
Above 600°C
Below 600°C
Multivariate mean in control sample by temperature class
95% confidence level ellipse
50% class contour
C
Canonical2
Canonical1
Archaeological CIELAB plots by temperature classification
25-200°C
400°C
600°C
800°C
m-FTIR re-classified to 400°C temp. class (n=13)
m-FTIR re-classified to 600°C temp. class (n=1)
Multivariate mean in control sample by temperature class
95% confidence level ellipse
50% class contour

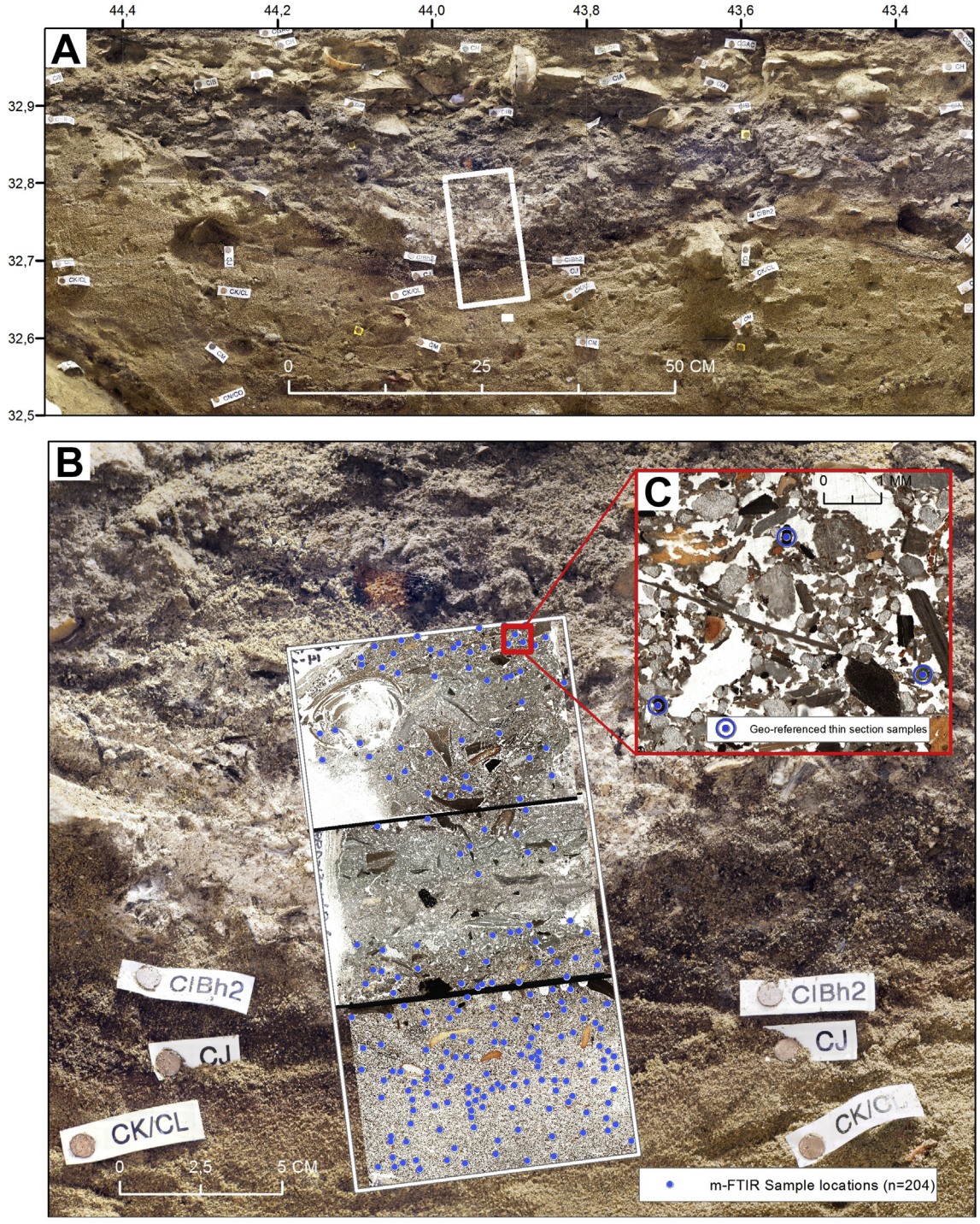

Fig. 11. (a) Ortophotographic overview of the combustion feature in the lower southern section of Blombos Cave (unit ClBh2). The white rectangle indicate where a block sample (BBC-13-14) was taken; (b) Close-up view showing the block sample location (white rectangle), the three thin sections from this block (BBC-13-14-a/b/c), as well as the spatial distribution of the micro-FTR and colourmetric measurements; (c) Close-up view of the high-resolution thin section scan, showing an example of 3 geo-referenced glauconite grains as they appear in a GIS software.

Fig. 10. Discriminant analysis of CIELAB colour values measured on glauconite grains in thin sections. (a) Principle Component Analysis (PCA) of the CIELAB colour measurements (n = 221) conducted on glauconite grains in thin sections control samples, classified by temperature (cf. Table B.2); (b) Canonical plot for a linear discriminant analysis of the CIELAB colour measurements (n = 203) conducted on glauconite grains in the archaeological thin sections (black crosses) (cf. Table B.3). The multivariate mean for each control sample temperature classes (25–200 °C, 400 °C, 600 °C and 800 °C) is indicated. The red and blue coloured crosses indicate whether the archaeological CIELAB plots were classified below or above 500 °C, based on the m-FTIR measurements conducted on the same grain. (c) Canonical plot identical to Fig. 10b, but here showing – by colour – the predicted temperature classification – based on their discriminant scores and proximity to the control group's multivariate mean – of each archaeological CIELAB colour plot. Green crosses indicates the glauconite measurements classified to the temperature range 25–200 °C, orange crosses to 400 °C, red crosses to 600 °C and black crosses to 800 °C. 13 colour measurements were originally classified to the 600 °C class, but considering their m-FTIR spectra they were not heated to above 500 °C. These 13 measurements were reclassified manually to the 400 °C temperature class (orange star). 1 colour measurement was originally classified to the 400 °C class, but considering its m-FTIR spectra they were heated to above 500 °C. This single measurement was reclassified manually to the 600 °C temperature class (red star). (For interpretation of the references to colour in this figure legend, the reader is referred to the web version of this article.)

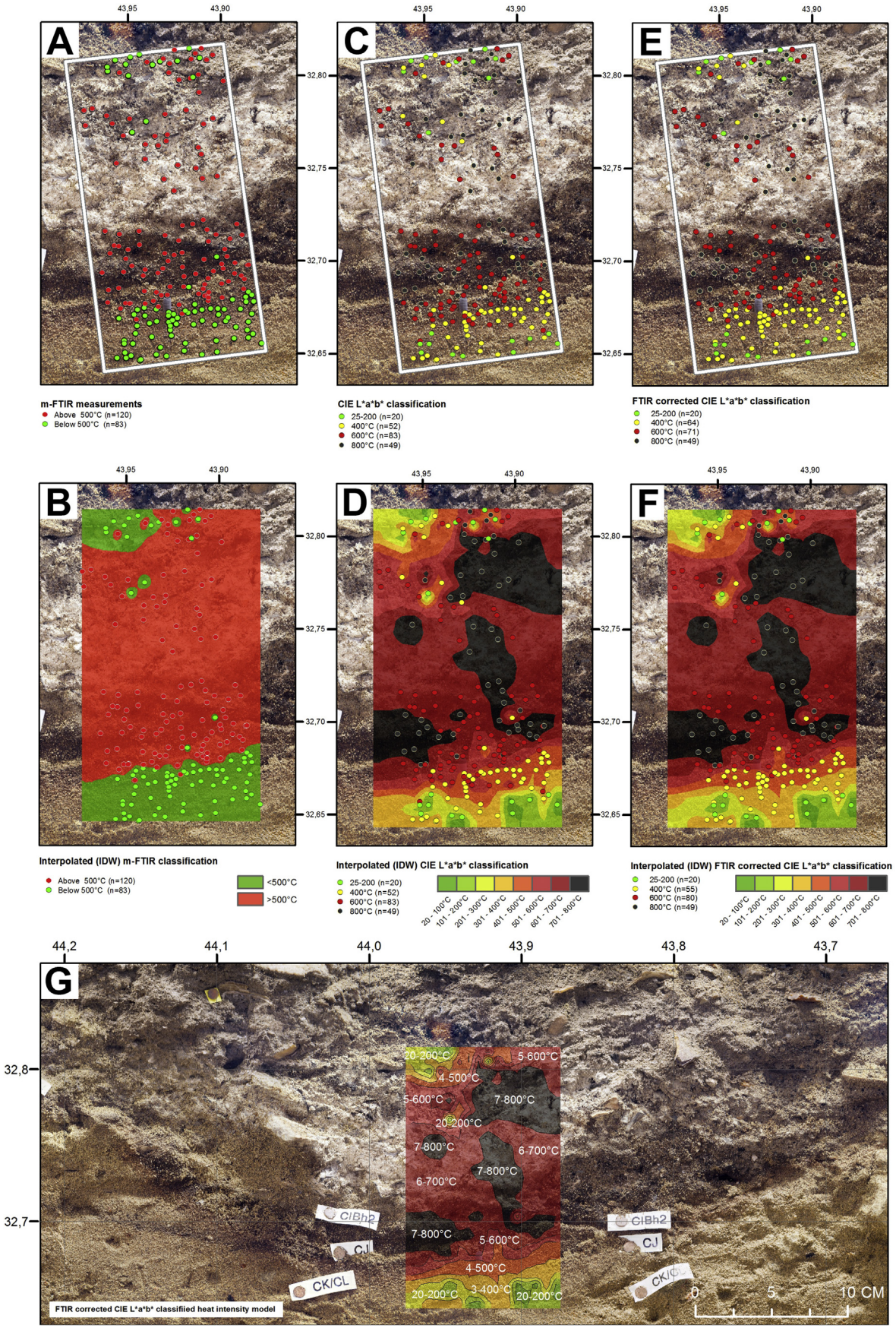
A
C
E
B
D
F
G
43,95
43,90
32,80
32,75
32,70
32,65
m-FTIR measurements
Above 500°C (n=120)
Below 500°C (n=83)
CIE L*a*b* classification
25-200 (n=20)
400°C (n=52)
600°C (n=83)
800°C (n=49)
FTIR corrected CIE L*a*b* classification
25-200 (n=20)
400°C (n=64)
600°C (n=71)
800°C (n=49)
Interpolated (IDW) m-FTIR classification
Above 500°C (n=120)
Below 500°C (n=83)
<500°C
>500°C
Interpolated (IDW) CIE L*a*b* classification
25-200 (n=20)
400°C (n=52)
600°C (n=83)
800°C (n=49)
20 - 100°C
101 - 200°C
201 - 300°C
301 - 400°C
401 - 500°C
501 - 600°C
601 - 700°C
701 - 800°C
Interpolated (IDW) FTIR corrected CIE L*a*b* classification
25-200 (n=20)
400°C (n=55)
600°C (n=80)
800°C (n=49)
44,2
44,1
44,0
43,9
43,8
43,7
32,8
32,7
20-200°C
4-500°C
5-600°C
7-800°C
6-700°C
3-400°C
ClBh2
CJ
CK/CL
FTIR corrected CIE L*a*b* classified heat intensity model
0
5
10 CM

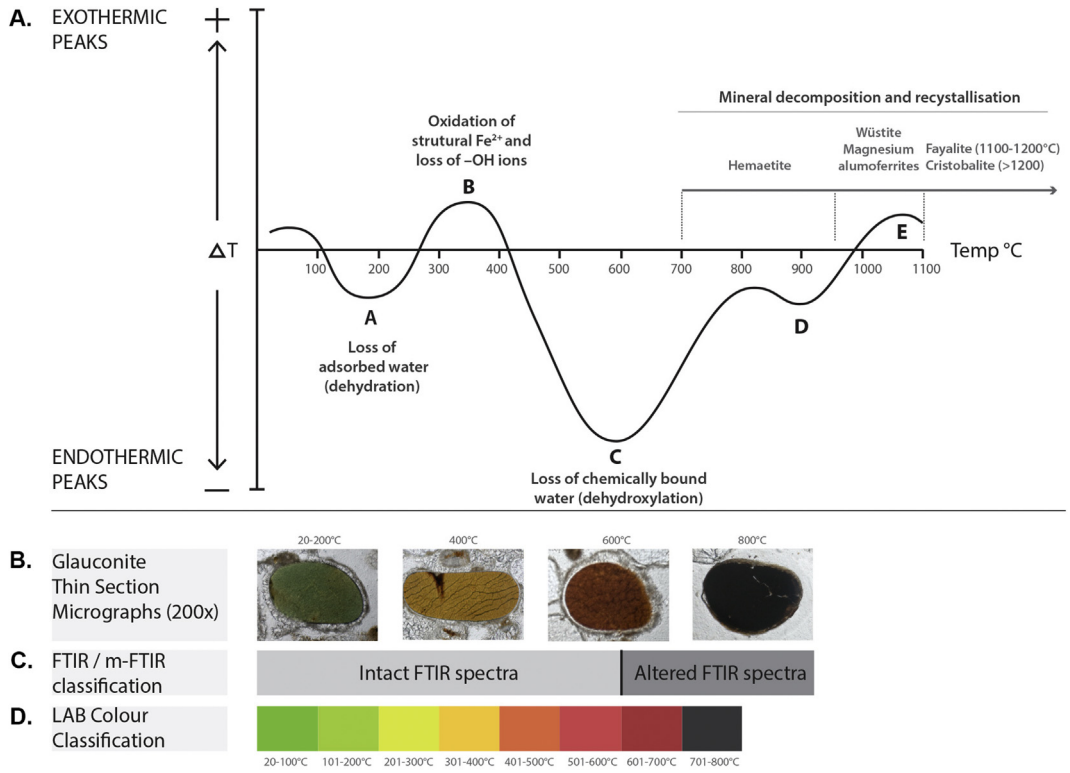

Fig. 13. Schematic overview of heat-induced optical and structural alterations of glauconitic minerals. (a) Idealized differential thermal analysis (DTA) curve for glauconitic minerals (revised after McRae, 1972); (b) Thin section micrographs of glauconite heated to various temperatures; (c) FTIR-based heat-classification of glauconite; (d) Colourimetric classification of glauconite.

humanly-controlled fire events. While an in-depth study of the thermal conductivity of the Blombos Cave sediments is not given here, there are several experimental studies that demonstrate how heat from a surface fire may transfer through soils and sediments, thereby altering the underlying substrate (Canti and Linford, 2000; Mallol et al., 2007; Miller and Sievers, 2012; March et al., 2014; Aldeias et al., 2016).

Most of these studies show that the sub-surface temperature depends on a range of variables that even under relatively controlled conditions may be difficult to predict fully (e.g. sediment type and content, grain size fraction and moisture content, temperature range, fire duration, compaction). Some core principles do seem to be valid for many types of open, informal fire settings; namely that the temperature of fire-heated sediment drops considerably as a function of burning temperature and depth below the heat source from a surface temperature of 950°C/600 °C, down to roughly 650 °C/450 °C at 2 cm depth, and c. 350 °C/200 °C at 6 cm depth (Aldeias et al., 2016). Somewhat higher temperatures have been reached at depths of up to 5 cm during very long fire experiments; 407 °C in sandy settings (peak after 31 h) and 506 °C in clay-rich settings (peak after 42 h) (Bennett, 1999).

The general principles of heat transfer through sediments in archaeological contexts can be used to guide an interpretation of the heat distribution pattern seen in the sampled Blombos Cave combustion feature (Fig. 12). For example, we note that the highest inferred temperature, according to the glauconite-classification scheme, is 600–800 °C. These temperatures are found in the ash-rich centre of the combustion feature and correspond to temperatures recorded in experimental hearths that primarily were fuelled by wood (for literature overview see Aldeias et al., 2016). Considering the thermal properties of sediments (low thermal conductivity) the heavily altered glauconite grains in the basal and central parts of the sampled combustion feature (Fig. 12f, zone A-D Fig. 15) must at one stage have been in direct contact with, or been very close to, a heat source. Given that the ash-rich area is > 10 cm deep, and ash is reported to be an efficient insulator (Canti and Linford, 2000), it seems highly unlikely that a single, short-lived fire would be able to produce enough heat to alter all the grains within this combustion feature simultaneously. Furthermore, the thickness of the ash in the sampled combustion feature from Blombos Cave is similar to that of the medium-sized hearths of Kebara Cave (Meignen et al., 2007) and the large combustion feature of Qesem Cave (Shahack-Gross et al., 2014), both of which were interpreted as the product of superimposed, successive burning events.

We may also note, that in the heavily burnt, ash-rich zone (B and D Fig. 15) the density of glauconite grains is lower than in the areas below the combustion feature (zone A Fig. 15). These low-density areas correlate positively with the regions that contain the highest input of calcareous ashes suggesting that the accumulation of ashy material occurred quickly, or at least much faster than the

Fig. 12. Interpolated (Inverse Distance Weighted, IDW) temperature maps based on the spatial distribution of heated and non-heated glauconite grains within the MSA hearth feature in unit CIBh2 of Blombos Cave (IDW settings: power 3; search radius: variable, number of points: 10; maximum distance: 60 mm). (a) Spatial distribution of glauconite grains by micro-FTIR based temperature classification (see Fig. 10); (b) Interpolated (IDW) temperature distribution model based on Fig. 12a; (c) Spatial distribution of glauconite grains by CIELAB based temperature classification (not corrected by m-FTIR spectra; (d) Interpolated (IDW) temperature distribution model based on Fig. 12c; (e) Spatial distribution of glauconite grains by CIELAB based temperature classification, corrected by m-FTIR spectra; (f) Interpolated (IDW) temperature distribution map based on Fig. 12e; (g) FTIR corrected CIELAB based temperature distribution model (based on Fig. 12f) compared to the general morphology of the MSA combustion feature.

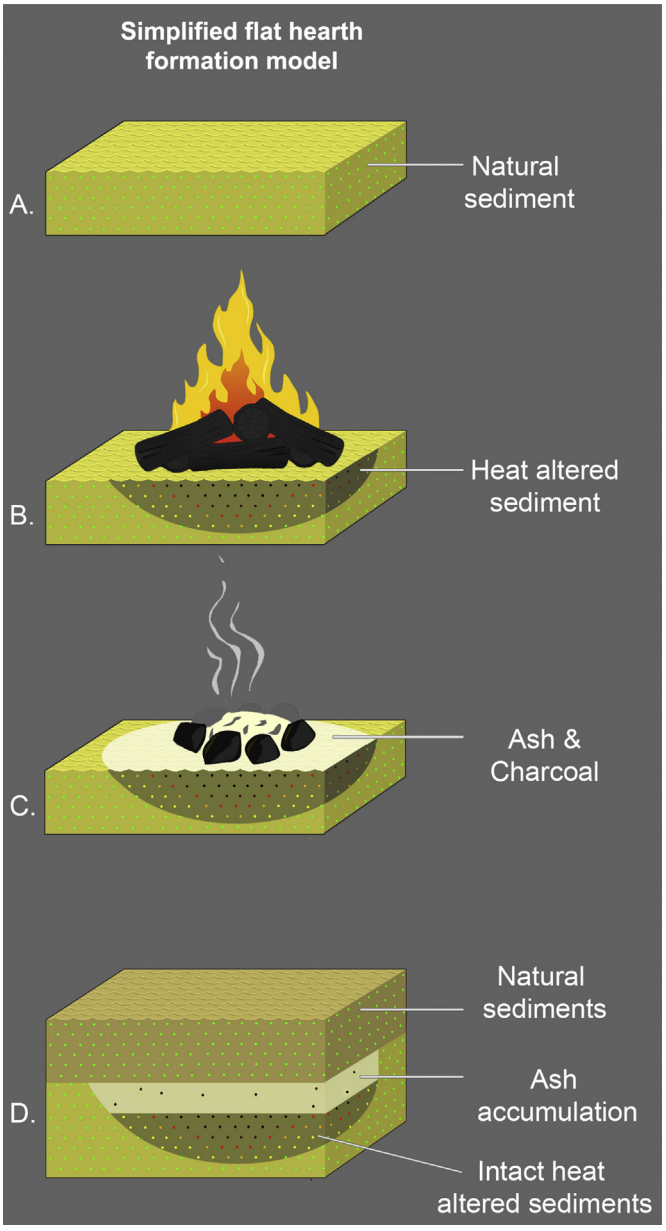

Fig. 14. Simplified flat hearth formation model showing the different stages and spatial distribution fire induced sediment alteration. Green dots represent un-heated glauconitic minerals. (a) Un-altered sediments; (b) Heat-altered sediments during fire activity; (c) Heat-altered sediments below ash and charcoal; (d) In-situ, single combustion feature buried under a layer of unaltered sediments. Note the preserved pattern of heat-altered sediments (represented by the colour of glauconitic grains) and the low grain density within the ash layer. (For interpretation of the references to colour in this figure legend, the reader is referred to the web version of this article.)

general depositional rate of glauconite (e.g. during a single burning event). However, we can also observe two zones within the combustion feature in which a mix of unaltered, moderately and heavily burnt glauconite grains have been introduced (zone C and E on Fig. 15). From preliminary micromorphological observations, we broadly relate the variation in grain alteration and grain density to markedly different ash-rich microfacies. While zone B and D in Fig. 15 appear to represent massive, undisturbed ash deposits (indicative of *in-situ* ash remains), zone C and E corresponds to more open-structured, ash-rich deposits with numerous micro-fragmented inclusions (indicative of a more reworked and possibly trampled deposits). The presence, location and spatial relationship between these microfacies suggest that the sampled hearth feature contains combustion residue from multiple, undisturbed burning events, separated by transitional phases of surface reworking, during which non-heated glauconite grains and other material got introduced.

It should here be noted that due to the non-reversible nature of heat-induced glauconite alteration, it would be more challenging to differentiate between multiple burning events within a stacked combustion that consist of a single, homogeneously burnt zone of deposits (e.g. no intermediate zones of mixed burnt material). These types combustion features would presumably have a very low number of glauconite grains incorporated, and the few grains present could potentially have been heated and reheated multiple times (March et al., 2014).

6. Concluding remarks

The Middle Stone Age sediments of Blombos Cave contain a high abundance of glauconitic minerals, and through heating experiments and the study of an intact combustion feature we have used the distribution and alteration of glauconite grains in thin sections to evaluate the effects of prehistoric fire on the underlying sedimentary substrate. In the archaeological thin sections, the glauconite grains were individually geo-referenced within a digital spatial environment (GIS), facilitating the production of heat distribution models that covered the original sampling area. Combined with orthophotographic section-wall images, these heat models allow us to visualise microscopic infrared measurements and optical observations in an intuitive way and to associate molecular alteration of grains in thin sections (micro-FTIR) with their original macroscopic field context.

From the nature and degree of heat-induced alteration and the spatial distribution of burnt deposits in the sampled MSA combustion feature in Blombos Cave, we conclude that:

1. The heat-altered sediments below the sampled MSA combustion feature are *in-situ.*
2. Multiple zones of calcareous (ash-rich) material in the centre of the combustion feature is minimally reworked.
3. Other parts of the combustion feature show mixing of both unburnt and heavily burnt sediments.
4. The ash-rich part of the combustion feature appears to have been formed during multiple, overlapping burning events that were separated by transitional phases of surface reworking.
5. The maximum temperature in the combustion feature was above 800 °C.

These results show that a thin-section based study of burnt deposits facilitates a robust evaluation of temporal resolution and spatial integrity of combustion features; aspects that must be clarified before any hearth or combustion feature may be linked to surrounding fire-related activity areas and overall site structure. Consequently, the multi-proxy, multi-scalar, and spatio-contextual framework we employ in this paper offers a highly robust and comprehensive approach to the analysis prehistoric burning events.

The single-grain, thin-section approach presented in this paper is directly applicable to other archaeological sites where glauconitic minerals occur, such as in other coastal caves of South Africa, e.g. Pinnacle Point (Karkanas et al., 2015), Klasies River Mouth (S. Mentzer personal communication) or in caves and rock shelters in France, e.g. Pech-de-l'Azé II (Goldberg, 1979) or Bordes-Fitte rock shelter (Aubry et al., 2014). For sites where glauconitic minerals are not present, the spatio-contextual framework, i.e. using high-

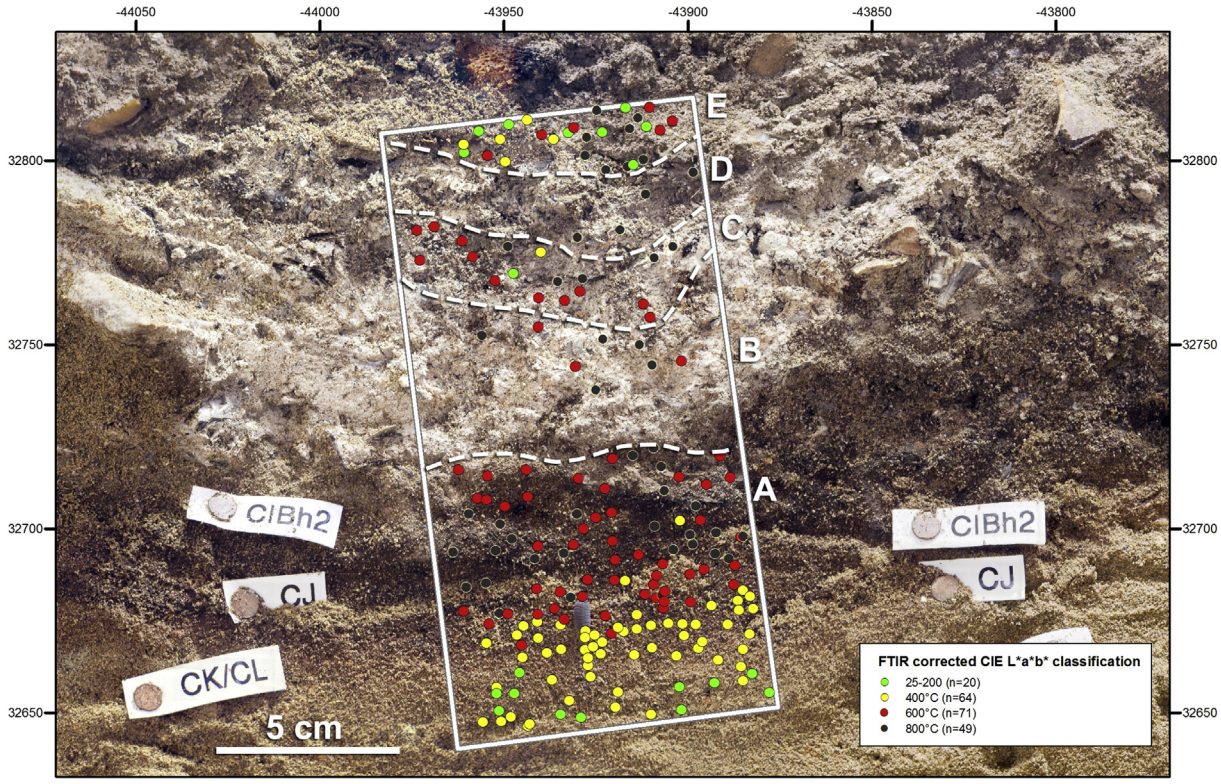

Fig. 15. The distribution of heated and unheated glauconitic projected on top a geo-referenced section photo of the sampled combustion feature. The variation in glauconite grain density corresponds broadly to five separate zones or microfacies; (A) Sandy deposits; (B,D) Low-density, massive ash deposits; (C) Medium density, burnt grains in calcareous deposits; (E) Medium density, burnt and unburnt grains in calcareous deposits.

resolution thin sections scans in a GIS environment, may easily be adapted to other sedimentary components that change their colour or composition when exposed to a heat source (e.g. bone, shell, and other clay minerals).

Acknowledgements

We thank Panos Kritikakis for producing the thin sections, Torstein Monsen for scanning of the thin sections and Sarah Meinekat and Lucie Leierer for the preparation of bulk samples. We would also like to thank Susan Mentzer for providing assistance and helpful information regarding the FTIR procedures and measurements, and Matthew Canti and Annika Burns for providing us with a copy of their glauconite comparative database. Financial support was provided to MMH by the Meltzer Research Fund (ID: 1303, 3718, 7604, 13107) and the Travel Fund for Doctoral Fellows at the Department of Archaeology, History, Cultural Studies and Religion, University of Bergen, Norway. The FTIR instrumentation was funded by a grant to CEM from the Deutsche Forschungsgemeinschaft (MI 1748/1-1). CSH was funded by European Research Council Advanced Grant, TRACSYMBOLS No. 249587, awarded under the FP7 program at the University of Bergen, Norway and by a National Research Foundation/Department of Science and Technology funded Chair at the University of the Witwatersrand, South Africa. The Publication fund for Open Access at the University of Bergen (BORA #5808) and the Department of Archaeology, History, Cultural Studies and Religion, University of Bergen, facilitated Open Access for this article.

Appendix A. Supplementary data

Supplementary data related to this article can be found at http://dx.doi.org/10.1016/j.jas.2017.06.008.

References

Affonso, M.T.C., Pernicka, E., 2001. Neolithic lime plasters and pozzolanic reactions. Are they occasional occurrences? Lux orientis. Archaeologie zwishen Asien und Europa, Festschrift für Harald Hauptmann zum 65, 9–13.
Aldeias, Vera, et al., 2016. How heat alters underlying deposits and implications for archaeological fire features: a controlled experiment. J. Archaeol. Sci. 67, 64–79.
Aubry, Thierry, et al., 2014. Middle-to-Upper Palaeolithic site formation processes at the Bordes-Fitte rockshelter (Central France). J. Archaeol. Sci. 52, 436–457.
Basso, Elena, et al., 2008. A particular temper: mineralogical and petrographic characterisation of ceramic fabrics with glauconitic inclusions. ArchéoSciences 93–97.
Bennett, Joanne L., 1999. Thermal alteration of buried bone. J. Archaeol. Sci. 26, 1–8.
Bentsen, S.E., 2012. Size matters: Preliminary results from an experimental approach to interpret Middle Stone Age hearths. Quat. Int. 270, 95–102.
Berna, Francesco, et al., 2007. Sediments exposed to high temperatures: reconstructing pyrotechnological processes in late bronze and iron Age strata at tel dor (Israel). J. Archaeol. Sci. 34, 358–373.
Berna, F., Goldberg, P., Horwitz, L.K., Brink, J., Holt, S., Bamford, M., Chazan, M, 2012. Microstratigraphic evidence of in situ fire in the acheulean strata of wonderwerk cave, northern Cape province, South Africa. Proc. Natl. Acad. Sci. 109 (20), E1215–E1220.
Canti, M.G., Linford, N., 2000. The effects of fire on archaeological soils and sediments: temperature and colour relationships. Proc. Prehist. Soc. 66, 385–395.
Chukanov, Nikita V., 2014. IR Spectra of Minerals and Reference Samples Data. Infrared Spectra of Mineral Species. Springer.
Dooley, John H., 2006. Glauconite. In: Kogel, Elzea, Jessica (Eds.), Industrial Minerals & Rocks: Commodities, Markets, and Uses. SME.
Eliyahu-Behar, Adi, et al., 2012. Iron and bronze production in Iron Age IIA Philistia: new evidence from Tell es-Safi/Gath, Israel. J. Archaeol. Sci. 39, 255–267.
Farmer Colin, V., 1974. Infrared Spectra of Minerals. Mineralogical Society, London, UK, p. 331.
Forget, Mathilde C.L., et al., 2015. Physical and mineralogical properties of experimentally heated chaff-tempered mud bricks: implications for reconstruction of environmental factors influencing the appearance of mud bricks in archaeological conflagration events. J. Archaeol. Sci. Rep. 2, 80–93.
Friesem, David E., et al., 2014a. Where are the roofs? A geo-ethnoarchaeological study of mud brick structures and their collapse processes, focusing on the

identification of roofs. Archaeol. Anthropol. Sci. 6, 73–92.
Friesem, David E., Zaidner, Yossi, Shahack-Gross, Ruth, 2014b. Formation processes and combustion features at the lower layers of the Middle Palaeolithic open-air site of Nesher Ramla, Israel. Quat. Int. 331, 128–138.
Goldberg, Paul, 1979. Micromorphology of Pech-de-l'Azé II sediments. J. Archaeol. Sci. 6, 17–47.
Goldberg, Paul, et al., 2012. New evidence on Neandertal use of fire: examples from Roc de Marsal and Pech de l'Azé IV. Quat. Int. 247, 325–340.
Grim, Ralph E., 1968. Clay mineralogy.
Hajpál, M., Török, Á., 2004. Mineralogical and colour changes of quartz sandstones by heat. Environ. Geol. 46, 311–322.
Heller-Kallai, L., Rozenson, I., 1980. Dehydroxylation of dioctahedral phyllosilicates. Clays Clay Miner. 28, 355.
Henry, Donald O., et al., 1996. Middle paleolithic behavioral organization: 1993 excavation of tor faraj, southern Jordan. J. Field Archaeol. 23, 31–53.
Henshilwood, Christopher S., 2005. Stratigraphic integrity of the middle Stone Age levels at Blombos cave. In: D'Errico, Francesco, Backwell, Lucinda (Eds.), From Tools to Symbols : from Early Hominids to Modern Humans ; in Honour of Professor Phillip V. Tobias. Witwatersrand University Press, Johannesburg.
Henshilwood, Christopher S., et al., 2001. Blombos cave, southern Cape, South Africa: preliminary report on the 1992–1999 excavations of the middle Stone Age levels. J. Archaeol. Sci. 28, 421–448.
Henshilwood, Christopher S., et al., 2011. A 100,000-year-old ochre-processing workshop at Blombos cave, South Africa. Science 334, 219–222.
Jacobs, Zenobia, et al., 2013. An improved OSL chronology for the Still Bay layers at Blombos Cave, South Africa: further tests of single-grain dating procedures and a re-evaluation of the timing of the Still Bay industry across southern Africa. J. Archaeol. Sci. 40, 579–594.
Karkanas, Panagiotis, et al., 2007. Evidence for habitual use of fire at the end of the lower paleolithic: site-formation processes at Qesem cave, Israel. J. Hum. Evol. 53, 197–212.
Karkanas, Panagiotis, et al., 2015. Interpreting human behavior from depositional rates and combustion features through the study of sedimentary microfacies at site Pinnacle Point 5-6, South Africa. J. Hum. Evol. 85, 1–21.
MacKenzie, K.J.D., Cardile, C.M., Brown, I.W.M., 1989. Thermal and moessbauer studies of iron-containing hydrous silicates. Part 7. Glauconite. ChemInform 20.
Malan, Jean Arnaud, 1990. The Stratigraphy and Sedimentology of the Bredasdorp Group. University of Cape Town, Southern Cape Province.
Malan, J.A., Viljoen, J.H.A., Siegfried, H.P., Wickens, J.D.V., 1994. Die geologie van die gebied Riversdal. Geological Survey of South Africa. Government Printer, Pretoria, 63 pp.
Mallol, Carolina, et al., 2007. Earth, wind, and fire: ethnoarchaeological signals of Hadza fires. J. Archaeol. Sci. 34, 2035–2052.
Mallol, Carolina, et al., 2013. The black layer of Middle Palaeolithic combustion structures. Interpretation and archaeostratigraphic implications. J. Archaeol. Sci. 40, 2515–2537.
March, Ramiro Javier, et al., 2014. Processes of formation and alteration of archaeological fire structures: complexity viewed in the light of experimental approaches. J. Archaeol. Method Theory 21, 1–45.
Marel, Van der, Willem, Herman, Hans, Beutelspacher, 1976. Atlas of Infrared Spectroscopy of Clay Minerals and Their Admixtures. Elsevier Publishing Company.
McRae, S.G., 1972. Glauconite. Earth-Science Rev. 8, 397–440.
Meignen, Liliane, Goldberg, Paul, Bar-Yosef, Ofer, 2007. He hearths at Kebara cave and their role in site formation processes. In: Bar-Yosef, O., Meignen, L. (Eds.), Kebara Cave Mt. Carmel, Israel. The Middle and Upper Paleolithic Archaeology. Part I. Peadbody Museum of Archaeology and Ethnology Harvard University, Cambridge, Massachusetts.
Mentzer, Susan M., 2012. Microarchaeological approaches to the identification and interpretation of combustion features in prehistoric archaeological sites. J. Archaeol. Method Theory 1–53.
Mentzer, Susan M., 2017. Hearths and combustion features. In: Gilbert, Allan S. (Ed.), Encyclopedia of Geoarchaeology. Dordrecht. Springer, Netherlands.
Miller, C.E., Sievers, C., 2012. An experimental micromorphological investigation of bedding construction in the middle Stone Age of Sibudu, South Africa. J. Archaeol. Sci. 39 (10), 3039–3051.
Miller, C.E., et al., 2016. Site-formation processes at elands bay cave, South Africa. South. Afr. Humanit. 29, 69–128.
Muller, Fabrice, et al., 2000. Dehydroxylation of Fe3+, Mg-rich dioctahedral micas: (I) structural transformation. Clay Miner. 35, 491–504.
Odin, Gilles S., 1988. Green Marine Clays: Oolitic Ironstone Facies, Verdine Facies, Glaucony Facies and Celadonite-bearing Rock Facies-a Comparative Study. Elsevier.
Odin, G.S., et al., 1988. Chapter D nature and geological significance of celadonite. In: Odln, G.S. (Ed.), Developments in Sedimentology. Elsevier.
Pavlyukevich, Yu G., Levitskii, I.A., Gailevich, S.A., 2005. Glauconite materials from Belarus and their application prospects. Glass Ceram. 62, 159–161.
Pestitschek, Brigitte, et al., 2012. Effects of weathering on glauconite: evidence from the abu tartur plateau, Egypt. Clays clay miner. 60, 76–88.
Ramaswamy, K., Kamalakkannan, M., 1995. Infrared study of influence of temperature on clay minerals. J. Therm. Anal. Calorim. 44, 629–638.
Shahack-Gross, R., et al., 2014. Evidence for the repeated use of a central hearth at Middle Pleistocene (300 ky ago) Qesem Cave, Israel. J. Archaeol. Sci. 44, 12–21.
Slonimskaya, M.V., et al., 1986. Interpretation of the IR spectra of celadonites and glauconites in the region of OH-stretching frequencies. Clay Miner. 21, 377.
Smykatz-Kloss, W., 1974. Differential Thermal Analysis: Application and Results in Mineralogy. Springer, Berlin Heidelberg.
Stevenson, Christopher M., Gurnick, Mary, 2016. Structural collapse in kaolinite, montmorillonite and illite clay and its role in the ceramic rehydroxylation dating of low-fired earthenware. J. Archaeol. Sci. 69, 54–63.
Vallverdú, Josep, et al., 2012. Combustion structures of archaeological level O and mousterian activity areas with use of fire at the Abric Romaní rockshelter (NE Iberian Peninsula). Quat. Int. 247, 313–324.
Villagran, Ximena S., et al., 2017. Buried in ashes: site formation processes at Lapa do Santo rockshelter, east-central Brazil. J. Archaeol. Sci. 77, 10–34.
Wadley, Lyn, 2006. The use of space in the late middle Stone Age of rose cottage cave, South Africa. In: Hovers, Erella, Kuhn, Steven L. (Eds.), Transitions before the Transition. Springer, US.
Weiner, Stephen, 2010. Microarchaeology : beyond the Visible Archaeological Record. Cambridge University Press, New York.
Wigley, Rochelle, Compton, John S., 2007. Oligocene to Holocene glauconite—phosphorite grains from the Head of the Cape Canyon on the western margin of South Africa. Deep Sea Res. Part II Top. Stud. Oceanogr. 54, 1375–1395.